

Lymphatic–stem cell crosstalk promotes tendon regeneration via Notch1–Srebp2–mediated cholesterol metabolism

Received: 31 March 2025

Accepted: 10 December 2025

Published online: 26 December 2025

 Check for updatesLiuqing Chen^{1,5}, Meilian Cai^{1,5}, Shuai Lin¹, Mingzhao Li¹, Zilu Zhu¹, Han Zhang¹, Hu Zhao², Chun Xu^{3,4} & Ruili Yang¹✉

Tendons, as bradytrophic tissues, exhibit limited healing capacity. The role of lymphatic vessels in tendon regeneration is largely overlooked. By comparing gene expression of the control and injured tendon cells from both neonatal and adult mice, we identify lymphatic vessels as key regenerative niche elements. Using the Transparent Embedding Solvent System for clearing in *Prox1-Cre^{ERT2}*; tdTomato mice, we find that lymphatic signaling was activated following tendon injury, directing the fate of distinct tendon stem/progenitor cell (TSPC) subsets. Mechanistically, the glycoprotein Reelin secreted from lymphatic endothelial cells (LECs) triggers VLDLR-dependent phosphorylation of DAB1 in TSPCs. Activated DAB1 binds to NOTCH1 at the tyrosine Y-200 residue, initiating Srebp2-mediated cholesterol metabolism. Functionally, *Reln^{-/-}* mice and *Prox1-Cre^{ERT2}*; *Reln^{fl/fl}* mice exhibit impaired tendon regeneration, underscoring the critical role of Reelin signaling. Furthermore, a slow-release Reelin delivery system established using mesoporous silica nanoparticles enhance tendon regeneration in mice and rabbits. These findings highlight the key role of lymphoangiocrine signaling in determining TSPC fate during tendon regeneration. Overall, this study provides a foundation for promoting tissue regeneration by targeting lymphatic signals.

Tendon injuries, caused by overuse or age-related degeneration, account for nearly half of musculoskeletal disorders and are frequently linked to poor clinical outcomes¹, creating a substantial burden on global healthcare systems². The main challenge is fibrotic scarring in healed tendons, which disrupts matrix continuity and impairs function. Tendons are composed primarily of dense extracellular matrix (ECM), maintained by tenocytes and tendon stem/progenitor cells (TSPCs)^{3,4}. Despite therapeutic advances, effective strategies to

improve tendon healing remain scarce, underscoring the need for a deeper understanding of TSPC biology and regulatory mechanisms^{5,6}.

TSPCs exhibit clonogenicity, self-renewal, and multilineage differentiation, enabling limited tendon homeostasis under physiological conditions. Transcription factors and signaling pathways associated with TSPCs were first identified in tendon development studies, which established *Scleraxis (Scx)* as a tendon progenitor marker^{7,8}. Advances in single-cell sequencing have revealed heterogeneity in TSPC

¹Department of Orthodontics, Beijing Key Laboratory of Digital Stomatology, NHC Key Laboratory of Digital Stomatology, NMPA Key Laboratory for Dental Materials, National Center for Stomatology, National Clinical Research Center for Oral Diseases, National Engineering Research Center of Oral Biomaterials and Digital Medical Devices, Peking University School and Hospital of Stomatology, Beijing, China. ²Chinese Institute for Brain Research, Beijing, China.

³Faculty of Medicine and Health, Sydney Dental School, The University of Sydney, Camperdown, NSW, Australia. ⁴Charles Perkins Centre, The University of Sydney, Camperdown, NSW, Australia. ⁵These authors contributed equally: Liuqing Chen, Meilian Cai. ✉e-mail: rui liyang@bjmu.edu.cn

populations, identifying different subtypes, such as *Nestin*⁺, *Tppp3⁺Pdgfra⁺*, *Cd146⁺*, and *Cd9⁺Cd271⁺* subpopulations, which play critical roles in tendon development and regeneration^{9–11}. Although progress has been made in defining early tendon formation, the cellular dynamics underlying differentiation, maturation, and scar formation during healing remain poorly understood.

Stem cell properties are regulated by specialized niches that provide signals essential for maintenance and differentiation. TSPCs reside within a unique niche enriched in ECM components, such as fibromodulin and biglycan, with low cellularity, which hinders repair after injury⁴. Although tendons are regarded as sparsely vascularized, they possess greater vascular complexity than previously believed. In particular, lymphatic vessels infiltrate repair tissue after injury, as shown in a rat tendon lesion model^{12,13}. Lymphatic vessels have been extensively studied in other tissues, such as the intestine, for their roles in fluid transport, immune cell trafficking, and signaling^{14,15}. However, their homeostatic and regenerative functions in tendons have not been fully examined. Reelin, a large extracellular glycoprotein traditionally associated with neuronal migration and cortical development^{16,17}, has also been detected in lymphatic vessels. In peripheral tissues, Reelin regulates cardiac growth and repair, epithelial cell proliferation, and intestinal crypt stability^{18,19}. It may also influence limb development and tissue regeneration; however, its mechanisms in tendons remain unclear²⁰.

In this study, we identified lymphatic vessels as a central signaling hub for tendon regeneration and TSPC fate determination. Specifically, lymphoangiocrine Reelin was found to activate Notch1-Srebp2-mediated cholesterol metabolism, preserving TSPC stemness and enhancing tendon repair. Furthermore, a slow-release Reelin delivery system based on mesoporous silica nanoparticles (MSNs) was shown to markedly improve tendon regeneration. These findings reveal significant interaction between lymphatic vessels and TSPCs, offering a promising strategy for tendon regeneration.

Results

Lymphatic endothelial cells (LECs) are a key component of the tendon stem cell niche

Neonatal tendons (before postnatal day 7) acquire functional recovery after injury, while adult tendons typically heal with fibrovascular scarring and persistent impairment²¹. To identify the molecular drivers of tendon regeneration and maturation, we compared gene expression in cells from control and injured tendons of neonatal and adult mice using single-cell RNA sequencing (scRNA-seq, Fig. 1A). The tendon-derived cells were classified into nine major cell clusters based on gene expression profiles (Figs. 1B–E and S1A–D). Cluster 0 showed high expression of tenogenesis-associated genes, including *Scx*, tenomodulin (*Tnmd*), tenascin-C (*Tnc*), and fibromodulin (*Fmod*)²². To examine the mechanisms of tendon maturation, we isolated tenogenic subset cluster 0 for uniform manifold approximation and projection-based clustering. Clusters were annotated using marker gene expression and gene set scores derived from predefined canonical stem cell, progenitor cell, and mature tenocyte genes (Figs. 1F, G and S1E). The cluster expressed stem cell markers lymphocyte antigen 6 complex, locus A (*Ly6a*) and Thy-1 cell surface antigen, was annotated as tendon stem cells (TSCs). The cluster exhibited the highest progenitor cell-associated gene set score, leading to its classification as tendon progenitor cells (TPCs). Another cluster with high expression of the ECM genes *Fmod* and thrombospondin-4 (*Thbs4*) for mature tendon cells was designated tenocytes (Figs. 1G and S1E). The stemness scores calculated based on the stemness-related gene set showed decreasing stemness scores from TSCs to tenocytes, which aligned with the subpopulation definitions (Fig. 1H). Furthermore, Monocle3 and CytoTRACE analysis confirmed differentiation path from TSCs through TPCs to tenocytes (Fig. 1I, J), suggesting the three distinct TSPC subsets transited from neonatal to adult tissue. Immunofluorescence staining

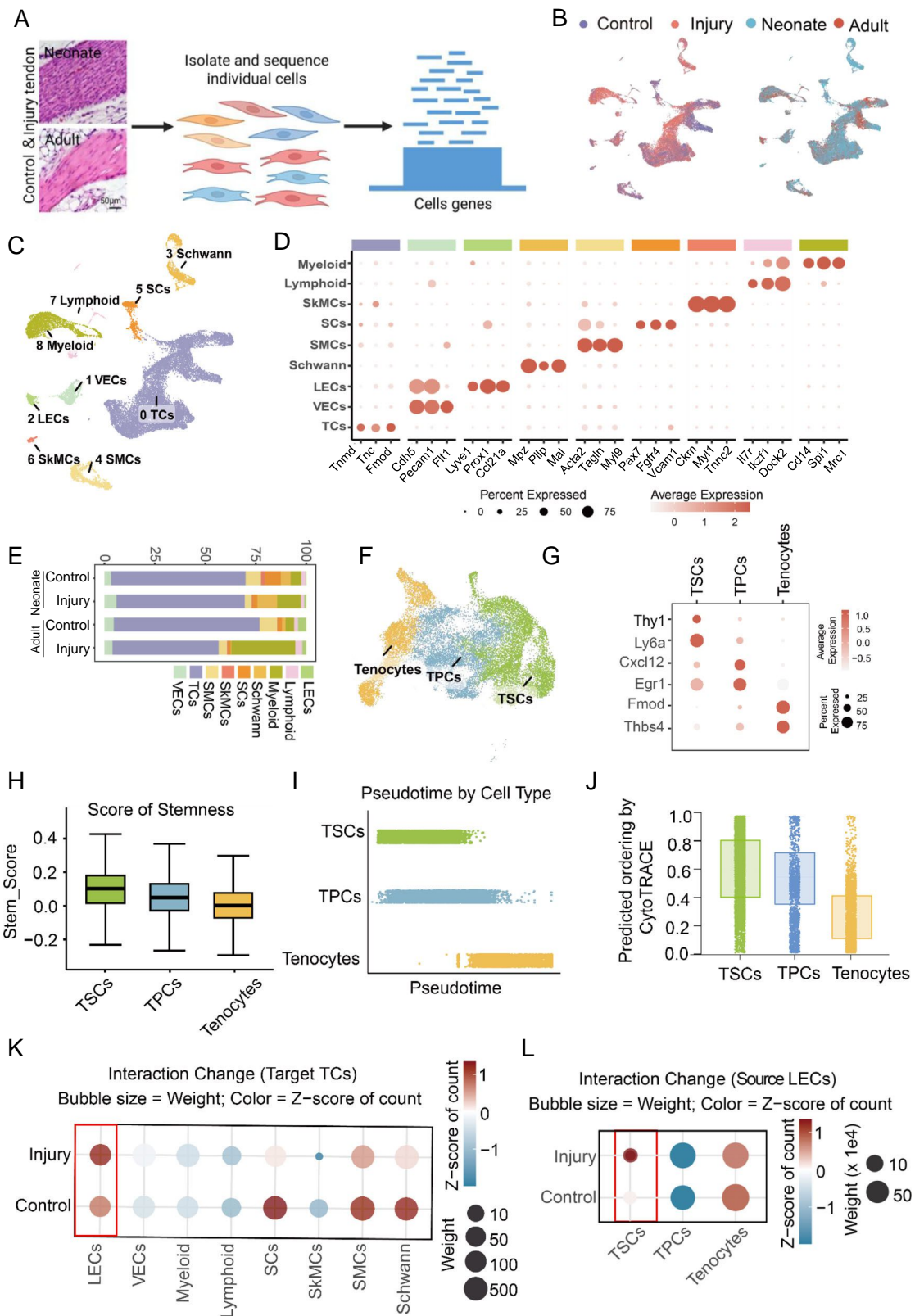
and gene expression on UMAP analysis demonstrated higher *Ly6a* levels in neonatal tendons, while higher *Scx* and proteoglycan 4 (*Prg4*) levels in adult ones (Fig. S1F, G).

The environment niche, where stem cells resident in, plays a crucial role in determining cell maintenance and fate²³. The cell-cell communication analysis highlighted increased interactions between LECs and tenogenic cells after injury compared with control one (Fig. 1K). To define this interaction mechanisms, we isolated tenogenic related subsets and endothelial cells for UMAP-based clustering and annotation (Fig. S1H–J). We further examined the interaction between LECs with three subpopulations of tenogenic cells and the results revealed specifically increased interaction between LECs and TSCs subsets after tendon injury (Fig. 1L). These findings indicate that lymphatics in tendons are key regulators of stem cell fate and tendon healing.

Lymphatic vessels expand after tendons injury

Tendons are composed of dense fibrous connective tissue, which render the lymphatic network difficult to visualize using conventional immunostaining¹³. To overcome this, we modified our previously reported Transparent Embedding Solvent System (TESOS)²⁴ for efficient tendon clearing and immunolabeling, enabling rapid, high-resolution, and three-dimensional (3D) confocal imaging (Fig. S2A). To analyze the lymphatic vessels in and around tendons, we used *Prox1-Cre^{ERT2}*; *tdTomato* mice and performed whole-mount imaging of the Achilles and Patellar tendons. This approach enabled visualization of *Prox1*-Tdtomato-positive lymphatic vessels in tendons (Fig. 2A, B; Supplementary Movies 1 and 2). To validate their identity, we performed immunolabeling using vascular endothelial and lymphatic vessel markers. *Prox1*-Tdtomato-positive lymphatic structures co-expressed the vascular endothelial marker CD31 and the LEC marker LYVE1 (Fig. S2B–D). Because vascular endothelial growth factor C (VEGF-C)/VEGF receptor 3 (VEGFR3) signaling is essential for lymphatic development and maintenance^{25,26}, we also demonstrated VEGFR3 expression in *Prox1*-Tdtomato-positive lymphatic vessels via immunostaining (Fig. S2E). Moreover, to analyze the interstitial fluid drainage function of these structures, we injected indocyanine green (ICG) and Evans blue to trace lymphatic flow. Subcutaneous ICG injections into the footpad showed uptake in Achilles tendons within 30 min as well as time-dependent clearance (Fig. S2F). Evans blue accumulated in LYVE1 positive lymphatic vessels of tendon tissues, which was also cleared over time (Fig. S2G)^{27,28}. These results indicate the functional lymphatic vessels distribution of tendon tissues. However, it was difficult to distinguish whether they distributed superficially on the tendon or within the tendon.

Next, to test LECs responses to tendon injury, we established an Achilles tendon transection model. Lymphatic vessels expanded after tendon injury in neonatal and adult mice, with increased *Prox1*-Tdtomato-positive and LYVE1-positive lymphatic vessels (Figs. 2C, D and S2H, I). Quantitative analysis also revealed elevated *Prox1* and *Lyve1* mRNA expression after tendon injury (Fig. S2J). As both the Achilles and patellar tendons are paratenon-sheathed tendons, comprising paratenon sheath and tendon substance. We therefore analyzed the precise distribution of expanded lymphatic vessels following injury. Our results demonstrated that in the control group, *Prox1*-Tdtomato and LYVE1-positive lymphatic vessels were mainly localized to the superficial tendon sheath. After injury, however, lymphatic vessels infiltrated to the tendon substance, as shown by the expression of COL1 α 1 and FMOD (Fig. S2K, L). Moreover, we treated injured tendons with VEGFR3-blocking antibody, which inhibited LYVE1-positive lymphatic vessel expansion (Fig. S2M). To model chronic tendinopathy, we induced Achilles tendon overuse. In this model, lymphatic expansion also occurred, as shown by *Prox1*-Tdtomato-positive vessels (Fig. S2N). Together, these results demonstrate the lymphatic vessels are mainly localized on tendon superficial sheath in homeostasis, while acute and chronic stress drive lymphatic expansion and growing into tendon.



Next, we examined how lymphatics contribute to tendon healing. CellChat analysis of TSPCs and LECs identified Reelin (*Reln*) signaling as the major pathway enriched after injury (Fig. 2E). Expression analysis also showed high *Reln* levels in LECs (Fig. 2F). Reelin protein has been reported to promote cardiac repair¹⁸. Immunostaining showed Reelin colocalization with the *Prox1*-tdTomato and LYVE1 in tendons. Reelin expression was also increased following tendon injury (Fig. 2G,

H). Moreover, the ELISA assay verified the levels of Reelin was increased after tendon injury (Fig. S20), indicating that lymphoangiocrine Reelin signaling is activated postinjury and may regulate tendon healing.

To assess the relevance of these findings in humans, we analyzed a published single-cell dataset of human tendons (Fig. S3)²⁹. We compared gene expression in tendon cells from healthy samples with cells

Fig. 1 | LECs was key component of the tendon stem cell niche. **A** Neonate and Adult tendons with or without tendon injury were isolated for single cell sequencing analysis. Created in BioRender. Yang, G. (2025) <https://BioRender.com/Svzdtg>. **B** The UMAP plots showed the clustering results of tendon tissues. **C** UMAP plot showing the clustering of tendon tissues, color-coded by cell cluster. Nine distinct cell clusters were identified, including tenogenic cells (TCs: *Tnmd*, *Tnc*, and *Fmod*), lymphatic endothelial cells (LECs: *Lyve1*, *Prox1*, and *Ccl21a*), vascular endothelial cells (VECs: *Cdh5*, *Pecam1*, and *Flt1*), Schwann cells (Schwann: *Mpz* and *Pllp*), smooth muscle cells (SMCs: *Acta2*, *Tagln*, and *Myl9*), satellite cells (SCs: *Pax7*, *Fgfr4*, and *Vcam1*), skeletal myocytes (SkMCs: *Ckm*, *Myl1*, and *Tnnc2*), myeloid cells (Myeloid: *Cd14*, *Spil*, and *Mrc1*) and lymphoid cells (Lymphoid: *Il7r*, *Ilkzf1*, and *Dock2*). **D** The bubble map showed marker genes expression, with redder colors indicating higher expression levels. Node size was proportional to the number of cells in each cluster. **E** The bar chart showed the percentages of cell clusters in control and injured tendons of neonatal and adult groups. **F–J** Sub-clustering of tenogenic related cells. **F** The UMAP plot of tenogenic cells colored by clusters. A

variety of distinct cell clusters were identified, including tendon stem cells (TSCs: *Thy1* and *Ly6a*), Tendon progenitor cells (TPCs: *Cxcl12* and *Egr1*) and mature tendon cells (Tenocytes: *Fmod* and *Thbs4*). **G** The bubble plot showed the marker genes expression of the three clusters, with redder colors indicating higher expression levels. **H** The box plot illustrated the score of stemness, the lower the score, the higher the degree of differentiation. The center line denoted the median; the upper and lower bounds of the box represented the 25th and 75th percentiles; the whiskers referred to the data points within 1.5 times the interquartile range from the box. TSCs (n:8878), TPCs (n:6806), Tenocytes (n:4925). **I** The pseudotime trajectory plot as predicted by monocle3. **J** The bar chart showed the CytoTRACE score. The lower the score, the higher the degree of differentiation. **K** The bubble plot depicted the interaction between indicated cell populations in control and injury groups, as predicted by CellChat. **L** Interactions between tenogenic cell subsets with LECs. Bubble size was proportional to the interaction weight and bubble color was proportional to the Z-score of interaction count.

from pathologic samples at 3 days postinjury (dpi), 10 dpi, and 12 weeks postinjury (wpi) (Fig. S3A–D). CellPhoneDB analysis revealed significant interactions between tenogenic cells and LECs (Fig. S3E). LECs count increased in pathologic samples at 10 dpi (proliferative phase) and 12 wpi (remodeling phase) (Fig. S3F). Interaction strength between tenogenic cells and LECs was higher at 10 dpi and 12 wpi compared with 3 dpi (Fig. S3G). Differential gene pathway enrichment analysis showed that ECM-receptor interaction signaling was upregulated in injured human tendons relative to healthy ones (Fig. S3H). These findings support increased lymphatic signaling involvement in tendon injury.

Reln signaling supports tendon regeneration

To examine the role of *Reln* signaling in tendon regeneration, we bred *Reln*^{-/-} mice (Fig. S4A). Their Achilles, Patellar, and tail tendons appeared hypoplastic and more translucent compared with controls. Additionally, histological analysis showed reduced collagen density and fewer cells in *Reln*^{-/-} mice tendons relative to controls (Figs. 3A and S4B). To evaluate *Reln* signaling in tendon healing, we created Achilles tendon transection defects in neonatal control and *Reln*^{-/-} mice. By 4 weeks postoperatively, controls regained near-normal function, whereas *Reln*^{-/-} mice showed limited regeneration, restricted mobility, and longer, narrower hind paw prints. Achilles functional index (AFI) values were lower in *Reln*^{-/-} mice compared with controls (Fig. 3B). Newly formed tendons in control mice displayed well-organized, abundant collagen fibers, whereas *Reln*^{-/-} mouse tissues contained sparse, fibrocartilage-like structures with fewer, disorganized collagen fibers, as shown via hematoxylin and eosin (H&E) and Masson's trichrome staining (Fig. 3C). Polarized light microscopy confirmed thinner collagen fibers and reduced extracellular matrix deposition in newly formed *Reln*^{-/-} tissues (Fig. S4C, D). Scanning electron microscopy (SEM) and transmission electron microscopy (TEM) revealed thinner, disorganized collagen fibers with decreased average diameter and density in *Reln*^{-/-} mouse tendons compared with controls (Fig. 3D). Magnetic resonance imaging (MRI) with sagittal T2-weighted scans showed low-intensity, homogeneous signals with clear margins in control newly formed tendons but irregular and heterogeneous high-intensity signals in *Reln*^{-/-} tendons (Fig. 3E). The inflammation-related M1 macrophage markers inducible nitric oxide synthase (iNOS) elevated in the *Reln*^{-/-} repair group compared with the control repair group (Fig. S4E). Expression of M2 macrophage-related markers CD206 was lower in the *Reln*^{-/-} repair group (Fig. S4F). Mechanical property analysis using an Instron tension/compression system³⁰ revealed superior mechanical properties in control repaired tendons, which exhibited greater stress at failure and elastic modulus compared with *Reln*^{-/-} tendons (Fig. 3F, G). Expression of the lymphatic markers LYVE-1 was also reduced in *Reln*^{-/-} tendons compared with controls (Fig. S4G, H).

Collectively, these results demonstrate that *Reln* signaling is critical for tendon regeneration.

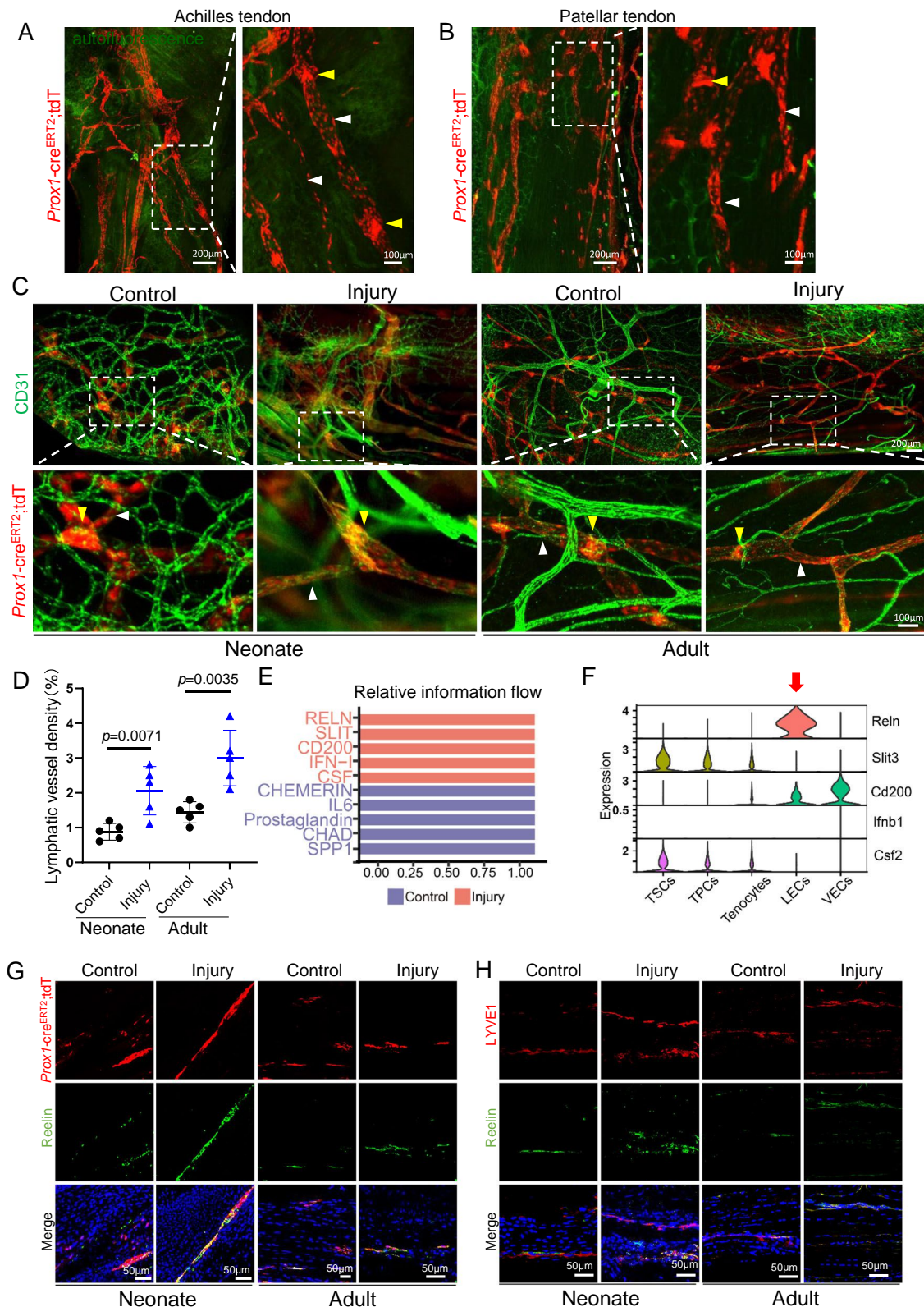
Reelin secreted by LECs controls tendon regeneration

To specifically assess the role of LEC-derived Reelin in tendon regeneration, we selectively deleted *Reln* in LECs using *Prox1*-Cre^{ERT2}; *Reln*^{fl/fl} (*Reln*^{cko}) mice. We failed to detect the expression of *Reln* in LECs of *Reln*^{cko} mice (Fig. S5A). Under baseline conditions, *Reln*^{cko} and control Achilles tendons showed no significant morphological or histological differences (Fig. 4A–D). We then established Achilles tendon transection defects in *Reln*^{fl/fl} and *Reln*^{cko} neonatal mice. At 4 weeks postoperatively, *Reln*^{cko} mice exhibited reduced mobility and function, with lower AFI values compared to the *Reln*^{fl/fl} group (Fig. 4B). Newly formed tendons in *Reln*^{cko} mice showed decreased cellularity and disorganized collagen compared with *Reln*^{fl/fl} tendons (Fig. 4C–F). SEM and TEM analyses confirmed thinner, more disordered fibers in the newly formed tissues of *Reln*^{cko} mice relative to control ones (Fig. 4G). MRI revealed hyperintensity signals in newly formed *Reln*^{cko} tendons (Fig. 4H). Functionally, newly formed *Reln*^{cko} tendons exhibited inferior mechanical properties (Fig. 4I, J). Additionally, the expression of the macrophage markers iNOS, and CD206 were elevated after tendon injury, while there was no significant difference between *Reln*^{fl/fl} and *Reln*^{cko} groups (Fig. S5B, C). LYVE1 expression in *Reln*^{cko} tendons showed a slight but nonsignificant decrease (Fig. S5D). These findings demonstrate that LEC-derived Reelin is essential for tendon regeneration, promoting tissue organization and functional recovery.

Vldlr⁺ population harbors neonatal TSPCs

Next, we explored how Reelin signaling regulates TSPC fate. Analysis the expression of Reelin receptors in TSPC subpopulations showed that *Vldlr* but not *Lrp8* (encodes ApoER2 protein) was highly expressed in TSCs (Fig. 5A). And the expression of *Vldlr* was upregulated in TSCs after injury (Fig. S6A). RT-qPCR and western blotting analyses confirmed higher *Vldlr* expression in neonatal TSPCs compared with adult ones (Fig. 5B, C), highlighting involvement of *Vldlr* in tendon maturation and healing.

Next, we generated *Vldlr*-Cre^{ERT2} mice using CRISPR/Cas9 and crossed them with R26R-tdTomato mice to generate *Vldlr*-Cre^{ERT2}; tdTomato mice. Lineage tracing after tamoxifen induction at P3–P5 showed that Tomato⁺ cells contributed 4.55% ± 1.77% to 36.48% ± 7.54% of *Col1a1*⁺ tendon cells from 7 days to 3 months during tracing (Fig. 5D, E). In contrast, when tamoxifen was injected at 1 month and traced for 3 months, Tomato⁺ cell proportions in tendons did not change significantly (Fig. 5F, G). Following tendon injury in Achilles tendon, most Tomato⁺ cells infiltrated the lesion and integrated into a FMOD-rich matrix at 30 days after injury (Fig. 5H). These results indicate that *Vldlr*-Tomato⁺ cells contribute substantially to tendon development and injury repair.



To explore the role of *Vldlr* in tendon regeneration, we sorted *Vldlr*-Tomato⁺ and *Vldlr*-Tomato⁻ tendon cells after 7 days of tamoxifen induction at P3–P5 (Fig. S6B). *Vldlr*-Tomato⁺TSPCs displayed higher proliferation, as indicated by an increased in Ki67⁺ cell count (Fig. 5I). *Vldlr*-Tomato⁺TSPCs also demonstrated a higher capacity for tenogenic differentiation, as shown by Sirius red and Masson trichrome staining (Fig. 5J). Transplantation of

Vldlr-Tomato⁺TSPCs into Achilles tendon transection model using ultraviolet-cured gelatin-methacryloyl (GelMA) as scaffolds revealed superior regenerative capacity. More organized fibers, abundant cells, and collagen deposition were detected in *Vldlr*-Tomato⁺TSPCs transplantation group, as shown via H&E and Masson trichrome staining (Fig. 5K). Overall, *Vldlr*-Tomato⁺ TSPCs displayed a higher capacity for tenogenesis and injury repair.

Fig. 2 | The lymphatic vessels were expanded after tendon injury. A, B The lymphatic vessels labeled by PROX1 in Achilles tendon and Patellar tendon using *Prox1-Cre^{ERT2}*; tdTomato mice, as presented by projection of 3D images after TESOS clearing. **C** The co-immunolabelling of *Prox1-Cre^{ERT2}*; tdTomato positive lymphatic vessels and CD31 in neonatal and adult Achilles tendon with or without tendon injury after 7 days, assessed by projection of 3D images after TESOS clearing. **D** The semi-quantitative analysis of tdTomato positive lymphatic vessels density in the indicated groups. **E** The top 5 significant signaling pathways based on the different genes between the control and injury groups. Those shown in red were higher

enriched in the injury sample. **F** The violin plots showed the increased 5 genes expression after injury in TSCs, TPCs, tenocytes, LECs and VECs. **G** The expression of Reelin in neonatal and adult tendons with or without tendon injury, presented by immunofluorescence staining in sectioned tendon tissue from *Prox1-Cre^{ERT2}*; tdTomato mice. **H** The expression of Reelin and LYVE-1 in neonatal and adult tendons with or without tendon injury. White triangle: lymphatic vessels; Yellow triangle: lymphatic valves. Each dot represents one individual replicate (n = 5 biological replicates per group in **D**). Statistical significance was analyzed by unpaired T test between control and injury groups at different ages, respectively.

Histological spatial analysis showed more VLDLR positive tendon cells located near lymphatic vessels, with this localized abundance increasing after tendon injury (Fig. S6C, D). The proliferation of VLDLR positive tendon cells was increased after injury compared with control ones. Additionally, compared with VLDLR positive tendon cells distant from lymphatic vessels, those adjacent ones showed higher proliferation index. Moreover, the nonproliferating VLDLR positive cells were located relatively farther from lymphatic vessels than the proliferating cells (Fig. S6E–H). In *Reln^{cko}* mice, the proliferation of VLDLR positive cell was also reduced (Fig. 5L), implicating lymphatics as a signaling hub to maintain TSPC properties. To validate the effects of Reelin on TSPCs, TSPCs were treated with recombinant Reelin protein. The results showed that Reelin treatment promoted TSPC proliferation (Fig. S6I) and tenogenic differentiation (Figs. S6J, K). Following transplantation of GelMA scaffolds loaded with TSPCs or Reelin-treated TSPCs into nude mice, better-organized collagen fibers were observed in the Reelin-treated group (Fig. S6L). These findings demonstrate that Reelin enhances TSPC proliferation and tenogenesis, supporting tendon regeneration.

Reelin activates Notch1–Srebp2-mediated cholesterol metabolism

Next, we investigated how Reelin signaling regulates TSPC stemness. Expression and phosphorylation of disabled-1 protein (DAB1), a key downstream effector of Reelin, were increased after Reelin treatment (Fig. 6A). Reelin binds its receptors, recruiting DAB1 to the NPXY internalization motif of VLDLR and inducing tyrosine phosphorylation³¹. Consistent with this process, *Vldlr* levels in TSPCs increased in a time-dependent manner following Reelin treatment (Fig. S7A). *Dab1* knockdown reversed Reelin-induced tenogenic differentiation, as shown via Masson trichrome and Sirius red staining (Figs. 6B, C and S7B). These results indicate that Reelin enhances tenogenesis through DAB1 phosphorylation.

Bulk RNA sequencing comparing *Vldlr* positive and *Vldlr* negative TSPCs revealed Notch1 pathway enrichment in *Vldlr* positive cells (Figs. 6D and S7C–E). Levels of Notch1 and its active form, the Notch1 intracellular domain (NICD), were substantially reduced in *Vldlr* TSPCs (Fig. 6E). Reelin treatment elevated NICD levels and Notch1 nucleus translocation, which were suppressed by *Dab1* knockdown, analyzed by western blotting and immunofluorescence (Fig. 6F–H). Coimmunoprecipitation analysis revealed a NICD–DAB1 interaction, which was enhanced by Reelin treatment, but was partially disrupted after *Dab1* siRNA treatment (Fig. 6I). DAB1 is phosphorylated at multiple tyrosine (Y) residues, including Y185, Y198, Y200, Y220, and Y232³², which is critical for NICD protein stability³³. The site-directed mutations of Y185F, Y198F, and Y200F, replacing tyrosine with a phenylalanine (F) to prevent phosphorylation at the tyrosine site, impaired DAB1's ability to stabilize NICD. Additionally, Reelin-induced NICD binding was inhibited by these mutations (Fig. 6J). Notably, the Reelin-induced decrease in NICD ubiquitination was inhibited with the Y200F mutation, but not the Y185F and Y198F mutations (Fig. 6K). Thus, Reelin promotes DAB1 phosphorylation at Y200, activating Notch1 signaling. Functionally, Reelin-induced tenogenic differentiation of TSPCs were attenuated by the Notch1 inhibitor DAPT treatment (Fig. S7F, G).

VLDLR, together with LDLR and low-density lipoprotein receptor-related protein 1 (LRP1), is key endocytic receptor, recognizing apolipoprotein E (apoE)-containing lipoproteins and contributing to cholesterol metabolism and transport³⁴. Notch1–Srebp2 was reported to regulate hematopoietic stem cell emergence³⁵. Reelin treatment elevated total cholesterol levels in TSPCs (Fig. 6L). Mechanistically, Reelin promoted apoE lipoprotein–VLDLR binding (Fig. S8A) and increased expression of *Srebp2*, the master regulator of cholesterol biosynthesis³⁴. This effect was partially blocked by DAPT treatment (Fig. 6M, N). Consistently, Reelin-induced cholesterol elevation was partially reversed by DAPT (Fig. 6O). *Srebp2* target genes, including 3-hydroxy-3-methylglutaryl-CoA reductase (*Hmgcr*) and 3-hydroxy-3-methylglutaryl-CoA synthase (*Hmgcs*), were upregulated by Reelin treatment (Fig. S8B, C). Notably, *Srebp2* knockdown using siRNA abrogated Reelin-induced cholesterol elevation (Fig. S8D, E). CUT&Tag-PCR assay revealed that Reelin enhanced NICD binding to the *Srebp2* promoter (Fig. S8F). These findings indicate that Reelin regulates cholesterol uptake through apoE–VLDLR interaction and de novo cholesterol synthesis via Srebp2 activation. Moreover, Reelin-induced enhancements in TSPC tenogenic differentiation were partially attenuated by *Srebp2* siRNA treatment (Fig. S8G, H). Thus, Reelin modulates cholesterol metabolism through Notch1–Srebp2 signaling, which preserves TSPC properties and supports tenogenic differentiation.

Slow-released Reelin promotes tendon regeneration in mice and rabbits

To enhance Reelin delivery for tendon regeneration, we used MSNs to enable Reelin loading and sustained release^{36,37}. TEM images showed spherical nanoparticles with a highly porous structure and uniform size (~190 nm). Nitrogen adsorption analysis, using the Barrett–Joyner–Halenda model, indicated average pore size of 33 nm based on the pore size distribution curve (Fig. S9A, B). Dynamic light scattering measurements suggested that MSNs had a hydrodynamic particle size of 200 nm and a zeta potential of –25 mV (Fig. S9C). Cone-shaped pores with large openings were visible on SEM images (Fig. 7A). With these pore features, MSNs achieved a Reelin loading concentration of 2 µg/mL and a loading efficiency of 40%. In protein release assays, ~60% of loaded Reelin was released over 72 h, confirming sustained delivery (Fig. 7B). MSNs also showed profound biocompatibility with TSPCs, which retained morphology, viability, and proliferation after nanoparticle exposure (Fig. 7C–E).

To investigate the regenerative effects of Reelin-loaded MSNs, they were embedded in a GelMA scaffold and applied to the Achilles tendon transection model. Reelin treatment partially improved tendon repair, and Reelin slow-release MSNs treatment resulted in superior tendon regeneration (Figs. 7F–H and S9D–F). Specifically, the Reelin slow-release MSNs showed improved mobility compared with Reelin or MSNs alone, as measured via the AFI (Fig. S9D). Newly formed tendons contained well-organized, abundant collagen fibers with a larger average diameter (Fig. 7G). MRI sagittal T2-weighted imaging confirmed that regenerated tendons in the Reelin slow-release MSNs group exhibited low-intensity, homogeneous signals with clear and smooth contours (Fig. 7H). Biomechanically, tendons treated with Reelin slow-release MSNs showed higher stress at failure and modulus

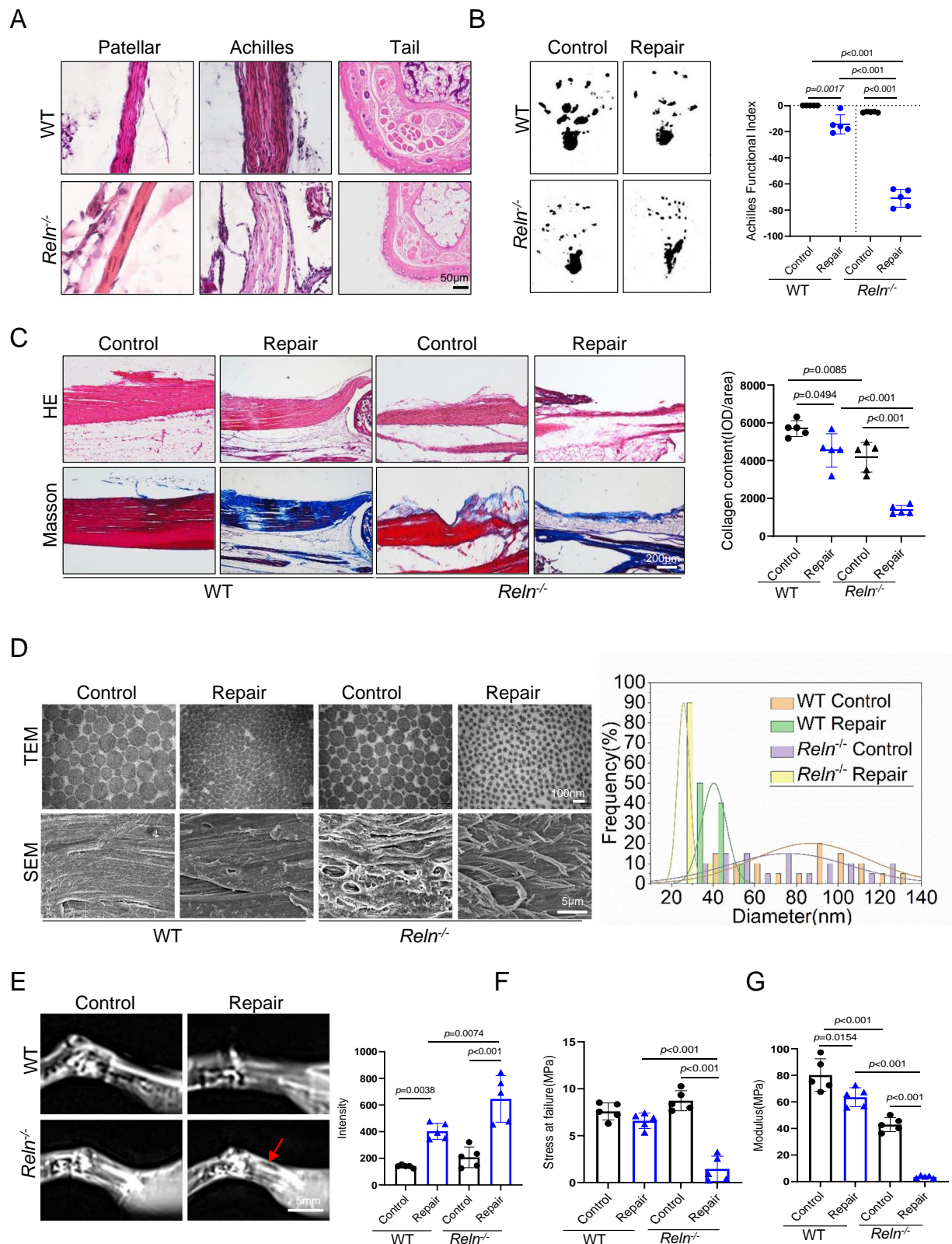


Fig. 3 | *Reln*^{-/-} mice showed deficiency of tendon regeneration. **A** HE staining of Patellar tendon, Achilles tendon and tail tendon in WT and *Reln*^{-/-} mice. **B** The footprints and AFI in control and 4 weeks after Achilles tendon transection of WT and *Reln*^{-/-} mice. **C** HE staining, Masson's trichrome staining and collagen content analysis in control and 4 weeks after Achilles tendon transection of WT and *Reln*^{-/-} mice. **D** The microstructure of tendons and collagen fiber diameters quantification in control and 4 weeks after Achilles tendon transection of WT and *Reln*^{-/-} mice, as assessed by SEM and TEM analysis. **E** The tendon contours and inflammation signaling in control and 4 weeks after Achilles tendon transection of WT and *Reln*^{-/-} mice, as analyzed by sagittal T2 MRI. **F, G** The stress at failure and modulus of Achilles tendon in control and 4 weeks after Achilles tendon transection of WT and *Reln*^{-/-} mice. Red arrow: indicate the inflammation signal. Each dot represents one individual replicate (n = 5 biological replicates in **B, C, E, F, G**). Statistical significance was analyzed by One-way ANOVA with Tukey's multiple comparisons test (**B, C, E, F, G**).

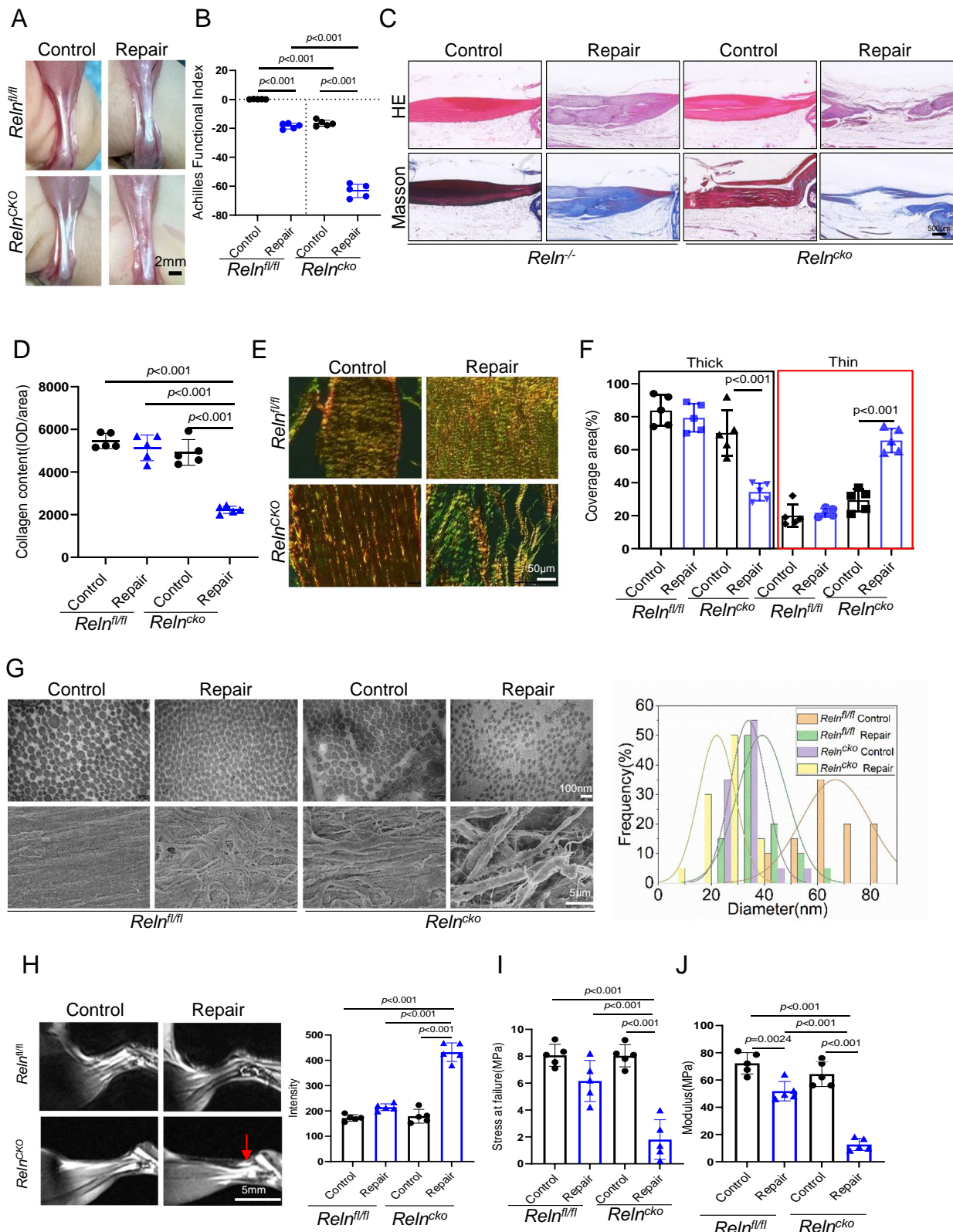
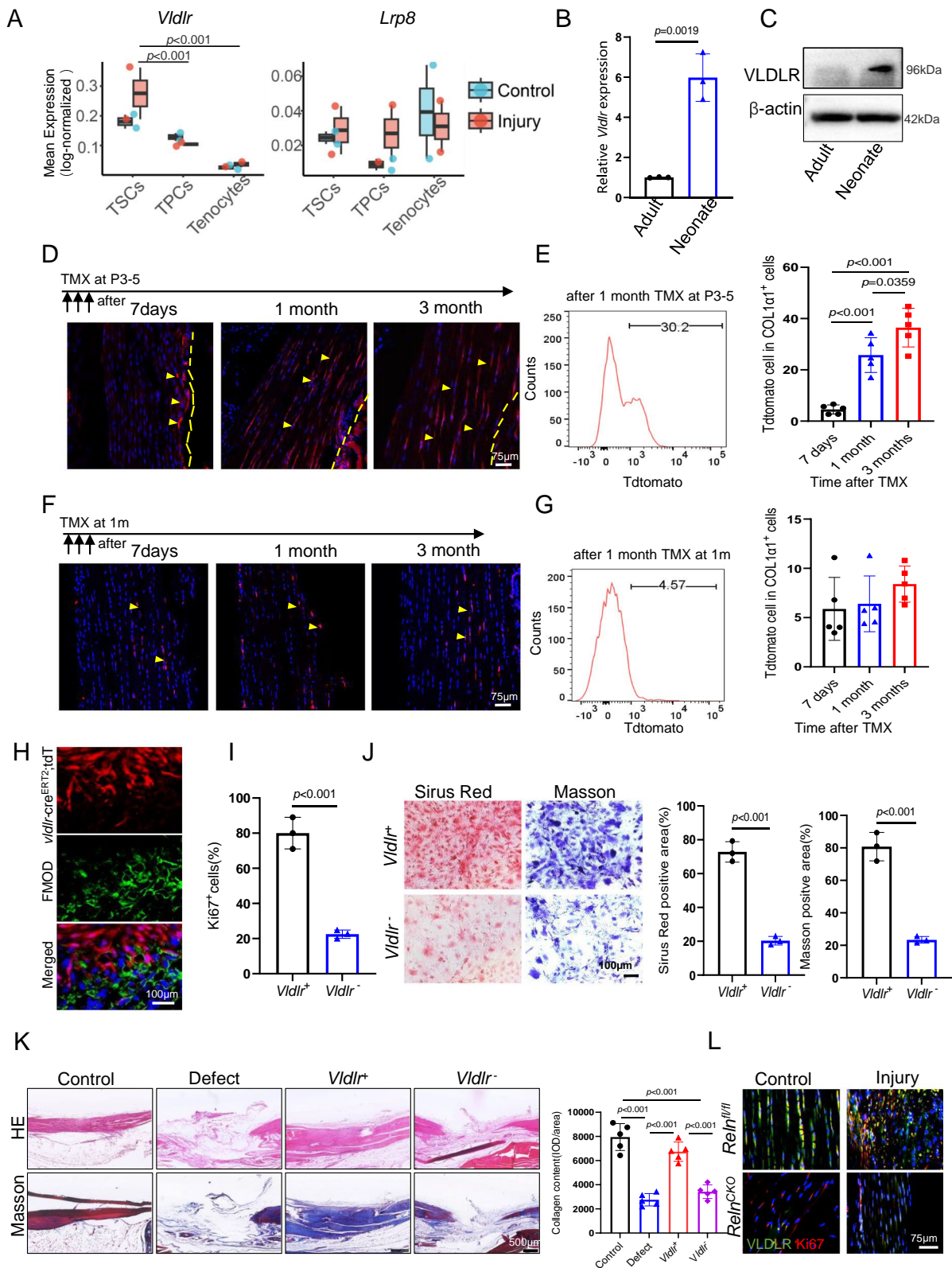


Fig. 4 | The Reelin signaling from LECs promoted tendon regeneration. **A** The macrostructure of Achilles tendon in control and repair groups of *Reln^{fl/fl}* and *Reln^{cko}* mice. **B** The AFI in control and repair groups of *Reln^{fl/fl}* and *Reln^{cko}* mice. **C** HE and Masson's trichrome staining in control and repair groups of *Reln^{fl/fl}* and *Reln^{cko}* mice. **D** The collagen content analysis in control and repair groups of *Reln^{fl/fl}* and *Reln^{cko}* mice. **E, F** The collagen amount and arrangement in control and repair groups of *Reln^{fl/fl}* and *Reln^{cko}* mice. **G** The microstructure of tendons and collagen fiber

diameters quantification in the control and repair groups of *Reln^{fl/fl}* and *Reln^{cko}* mice, assessed by TEM and SEM. **H** Sagittal T2 MRI imaging and intensity in control and repair groups of *Reln^{fl/fl}* and *Reln^{cko}* mice. **I, J** The stress at failure and modulus in control and repair groups of *Reln^{fl/fl}* and *Reln^{cko}* mice. Red arrow: indicate the inflammation signal. Each dot represents one individual replicate (n = 5 biological replicates per group in **B, D, F, H, I, J**). Statistical significance was analyzed by One-way ANOVA with Tukey's multiple comparisons test (**B, D, F, H, I, J**).



values (Fig. S9E, F). In rabbits, Reelin slow-release MSNs combined with TSPC transplantation enhanced functional tendon regeneration in Achilles tendon transection model (Fig. S9G–J). Collectively, these results show that Reelin-loaded MSNs promote tendon regeneration in mice and rabbits, underscoring their translational potential.

Overall, this study identifies lymphatic signaling hub in tendons, where LEC-secreted Reelin promotes TSPC stemness through

Notch1–Srebp2-mediated cholesterol metabolism. Functionally, we highlight the essential role of this lymphatic hub in tendon regeneration (Fig. S10).

Discussion

Tendon regeneration remains a major challenge, particularly in adults, where healing is dominated by fibrosis and impaired function. In

Fig. 5 | *Vldlr*⁺ TSPCs demonstrated superior tenogenic differentiation capacity.

A The expression of *Vldlr* and *Lrp8* genes in TSCs, TPCs and Tenocytes. The center line denoted the median; the upper and lower bounds of the box represented the 25th and 75th percentiles; the whiskers referred to the data points within 1.5 times the interquartile range from the box. Statistical significance was analyzed by One-way ANOVA with Tukey's post hoc test using R software. **B** The RNA expression of *Vldlr* in Neonate and Adult groups, analyzed by RT-qPCR analysis. **C** The expression of VLDLR in Neonate and Adult groups, assessed by western blotting. **D** Confocal imaging of tendon sections from *Vldlr*-Cre^{ERT2}, tdTomato mice that had been induced by tamoxifen at P3 of age. Mice were analyzed at 7 days, 1 months and 3 months after the induction. **E** Flow cytometry analysis of enzymatically dissociated tendon cells from *Vldlr*-Cre^{ERT2}, tdTomato mice that had been induced by tamoxifen at P3; Col1a1 were stained to indicate the tendon cells. **F** Confocal imaging of tendon sections from *Vldlr*-Cre^{ERT2}, tdTomato mice that had been induced by tamoxifen at 1 month of age. Mice were analyzed at 7 days, 1 months and

3 months after the induction. **G** Flow cytometry analysis of enzymatically dissociated tendon cells from *Vldlr*-Cre^{ERT2}, tdTomato mice that had induced by tamoxifen at 1 month; Col1a1 were stained to indicate the tendon cells. **H** Images of renewed *Vldlr*-tdTomato positive cells and FMOD expression in 30 d regenerated tendons. **I** The proliferation of *Vldlr*⁺ and *Vldlr*⁻ TSPCs, analyzed by Ki67 staining. **J** The Sirius red, Masson trichrome staining and semi-quantification in *Vldlr*⁺ and *Vldlr*⁻ TSPCs. **K** The HE staining, Masson trichrome staining and collagen content analysis of regenerated tendon in control, defects, *Vldlr*⁺ and *Vldlr*⁻ TSPCs transplant groups. **L** The expression of VLDLR and Ki-67 in the control and injured *Reln*^{fl/fl} and *Reln*^{cko} tendons, analyzed by immunofluorescence. Each dot represents one individual replicate (n = 3 biological replicates in **B**, **I**, **J**; n = 5 biological replicates in **E**, **G**, **K**). Statistical significance was analyzed by One-way ANOVA with Tukey's multiple comparisons test (**A**, **E**, **G**, **K**). Statistical significance was analyzed by unpaired Student's *t* test (**B**, **I**, **J**).

contrast, neonatal tendons regenerate effectively, likely through TSPCs³⁸. Notably, TSPC subset showed association with LECs, implicating a specialized niche component in tendon regeneration. Using TESOS-based tissue clearing and 3D confocal imaging, we visualized lymphatic networks in Patellar and Achilles tendons. These networks expanded after injury and acted as signaling hubs. It's reported that crypt lymphatics preserve intestinal stem cell stemness¹⁴, and skin lymphatics support hair follicle stem cells while contributing to skin regeneration and repair³⁹. These observations indicate that lymphatics act as stem cell niches under physiological and pathological conditions⁴⁰. We identified Reelin from LECs as a key regulator of TSPC stemness and differentiation. Following injury, Reelin expression in tendon lymphatics increased, functioning as a lymphoangiocrine signal supporting tendon repair. In *Reln*^{-/-} mice, newly formed tendons displayed reduced cellularity, disorganized collagen fibers, and impaired mechanical properties. Consistent with prior reports of *Reln*^{-/-} mice exhibiting neural defects and weight gain failure⁴¹, we also observed tendon developmental dysplasia, reduced lymphatic formation in *Reln*^{-/-} mice. A previous study noted reduced smooth muscle cell coverage and irregular diameters in lymphatic collecting vessels in *Reln*^{-/-} mice, despite normal in lymphatic capillaries⁴². To test the direct role of LEC-derived Reelin, we deleted *Reln* in lymphatics using *Prox1*-Cre^{ERT2}, *Reln*^{fl/fl} mice. The resulting *Reln*^{cko} mice exhibited impaired tendon regeneration despite normal tendon development and lymphatic formation, confirming that lymphatic-derived Reelin specifically regulated tendon regeneration. These findings also suggest that the impaired tendon regeneration, at least in *Reln*^{-/-} mice, may be partially regulated by the decreased lymphatic vessels. Other lymphatic endothelial paracrine factors, such as netrin-1, interleukin 33, and R-spondin 3^{14,43}, may also contribute to tendon regeneration and warrant further investigation.

In newly formed tendons of *Reln*-deficient mice, we also detected a higher abundance of pro-inflammatory M1 macrophages. This observation aligns with previous report demonstrating that macrophages isolated from *Reln*^{-/-} mice exhibit an increased propensity for M1 polarization⁴⁴. Our study further revealed that Reelin treatment enhances the functional properties of TSPCs. Notably, advancements in tissue regeneration may also be mediated by the role of stem cells or their secretomes, which have been shown to suppress pro-inflammatory responses and facilitate the resolution of tendon pathologies. Specifically, mesenchymal stem cells are known to secrete prostaglandin E2 (PGE2) and transforming growth factor- β (TGF- β), which could promote the activation of M2 macrophages⁴⁵. Additionally, lymphatic vessels, which function to drain extravasated fluid, antigens, and inflammatory mediators, may themselves modulate macrophage polarization⁴⁶. Collectively, whether Reelin regulates macrophages polarization directly or indirectly through modulating lymphatic function or the anti-inflammatory properties of stem cells, need further investigation.

The differentiation continuum from stem cells to tenocytes underscores dynamic gene and cellular function changes during maturation^{11,47,48}. Among the three subsets of tenogenic cells we classified, early-stage TSPCs with high *Vldlr* expression were identified as key regenerative cells. Functionally, these cells displayed strong self-renewal and tenogenic differentiation capacities. These data suggest that *Vldlr* represents a characteristic marker for TSPCs with robust tenogenic and regenerative potential. It was reported that *Nestin* was not only recognized as a characteristic marker for TSPCs, but also hold broader implication, which expression in other cells may also indicate multipotentiality⁴⁹. Given this, the specific role of *Vldlr*—particularly whether it is associated with multipotency in cell types beyond TSPCs (i.e., liver and adipose tissue)—requires further investigation.

Mechanistically, we identified Reelin driven regulatory axis involving DAB1 and Notch1. Reelin stabilized Notch1 by preventing ubiquitination and proteasomal degradation, mediated by phosphorylated DAB1^{50,51}. Among five putative tyrosine phosphorylation sites in DAB1³², Y200 was critical for stabilizing Notch1. This interaction illustrates the complex molecular crosstalk within the TSPC niche. We also revealed the link between Notch1 and cholesterol metabolism via the Srebp2 pathway. Reelin enhanced TSPC stemness and tenogenic differentiation through Srebp2-mediated cholesterol metabolism, implicating metabolic regulation as a potential therapeutic target for tendon repair. It's also reported that Srebp2 mediated cholesterol metabolism regulates hematopoietic stem cell emergence³⁵. However, the detailed mechanisms for cholesterol metabolism control the property of TSPCs need further to be elucidated.

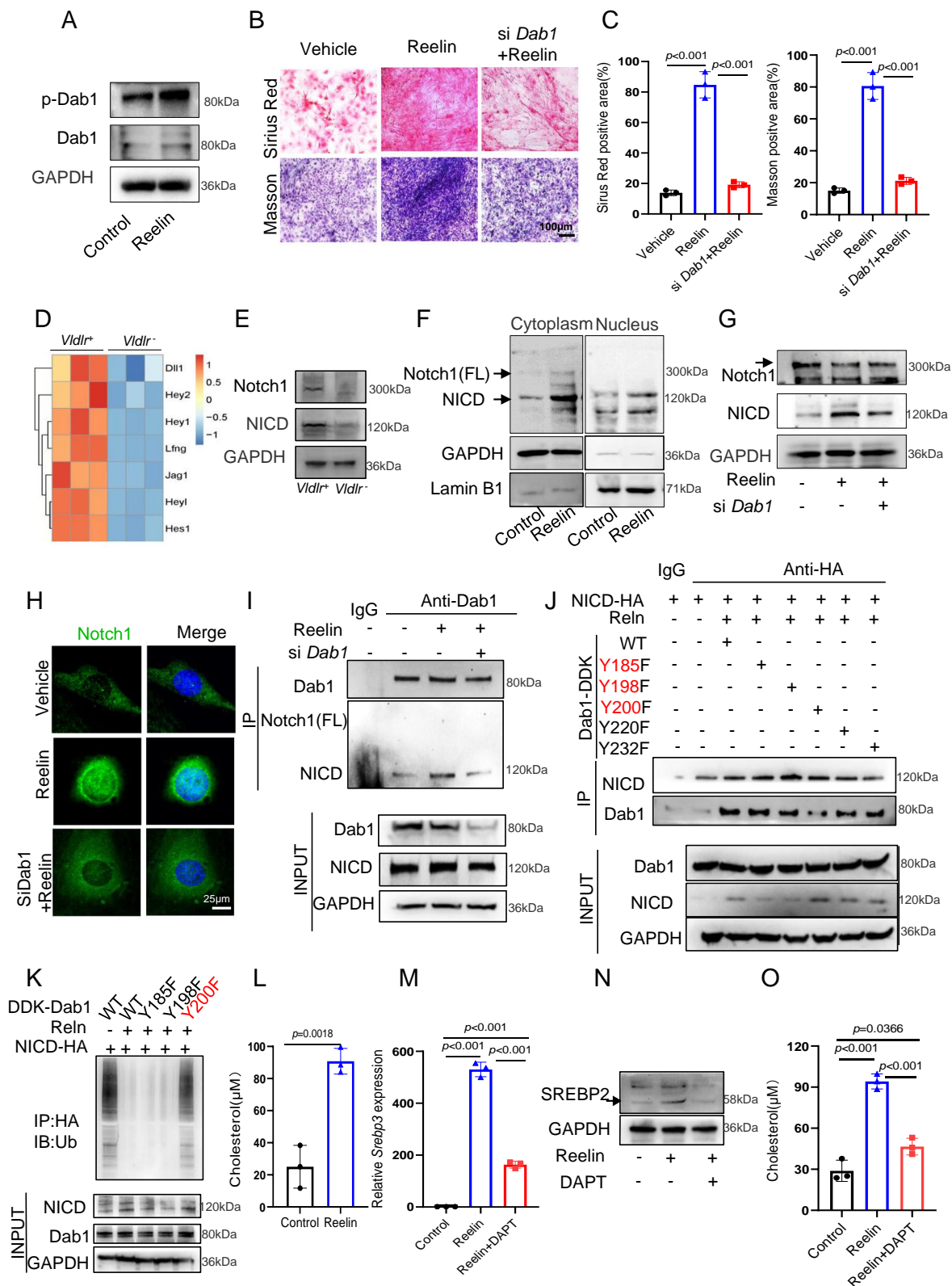
To translate these findings, we developed MSNs with a core-cone structure for controlled Reelin delivery. These nanoparticles showed high loading efficiency, and sustained release. In vivo, Reelin-loaded MSNs improved tendon strength, collagen organization, and cellular density after Achilles tendon injury. Application in rabbit models also demonstrated scalability and cross-species efficacy, supporting the translational potential.

In conclusion, this study establishes lymphatic signaling as a critical mechanism in tendon regeneration. The lymphoangiocrine Reelin regulates TSPC stemness and tenogenesis through Srebp2-mediated cholesterol metabolism. These findings not only provide insights into tendon biology but also introduce Reelin-loaded MSNs as a promising therapeutic strategy. Future research should investigate other lymphangiogenic factors and metabolic pathways to optimize regenerative therapies.

Methods

Animals

All experimental procedures performed in this study were following animal welfare ethical guidelines and approved by the Animal Use and Care Committee of Peking University (#LA20221488) and Animal Use and Care Committee of Chinese Institute for Brain Research(#CIBR-



IACUC-051), in accordance with the governmental regulations of China. Sex was not considered as a biological variable in this study. C57BL/6 (6–8 weeks) and BALB/c nude (8–10 weeks) mice were purchased from Charles River Laboratory (China). *Vldlr*-Cre^{ERT2} mouse line was generated at the Chinese Institute for Brain Research (CIBR) Genetic Manipulation Core. *Reln*^{-/-} mice (T009126) and *Reln*^{fl/fl} mice

(T012926) were purchased from GemPharmatech (China). *Prox1*-Cre^{ERT2} mice (Jax # 022075) and tdTomato mice (Jax # 007914) were obtained from the Jackson Laboratory (USA). *Prox1*-Cre^{ERT2} mice were breeding with tdTomato mice and *Reln*^{fl/fl} mice to get *Prox1*-Cre^{ERT2}; tdTomato and *Prox1*-Cre^{ERT2}; *Reln*^{fl/fl} mice. Rabbits (4 months) were purchased from Beijing Long'an Experimental Animal Breeding Center.

Fig. 6 | Reelin activated Notch1/Srebp2 mediated cholesterol metabolism.

A The expression of Dab1 and phosphorylated Dab1 (p-Dab1) in TSPCs treated with or without 1 μ g/mL Reelin, as assessed by western blotting. **B, C** The Sirius Red staining and Masson's trichrome staining of TSPCs in vehicle, Reelin and *Dab1* siRNA with Reelin treated groups. **D** The heatmap indicated the expression levels of genes related with Notch signaling in *Vldlr*⁺ and *Vldlr*⁻ TSPCs, analyzed by bulk RNA-seq. **E** The expression of NICD and Notch1 in *Vldlr*⁺ and *Vldlr*⁻ TSPCs, analyzed by western blotting. **F** The expression of Notch1 and NICD in cytoplasm and nucleus of control and Reelin treated groups, as assessed by western blotting. **G** The expression of NICD and Notch1 of TSPCs in vehicle, Reelin and *Dab1* siRNA with Reelin treated groups, as analyzed by western blotting. **H** The localization of Notch1 in vehicle, Reelin and *Dab1* siRNA with Reelin treated groups, as assessed by immunofluorescence staining. **I** Co-IP of Dab1 with NICD in vehicle, Reelin and *Dab1* siRNA with Reelin treated TSPCs groups. **J** Co-IP of Dab1 with NICD in HEK-293 cells,

which were transfected with indicated wild type (WT) or site mutated plasmids. **K** Co-IP evaluated the protein level of ubiquitinated NICD in HEK-293 cells, which were transfected with the indicated WT or site mutated plasmids and treated with MG132 (20 μ mol/L) for 6 h before cell harvested. **L** The cholesterol level in control and Reelin treated TSPC groups. **M** The mRNA level of *Srebp2* in vehicle, Reelin and DAPT with Reelin treated groups, analyzed by RT-qPCR. **N** The expression of SREBP2 of TSPCs in vehicle, Reelin and DAPT with Reelin treated groups. **O** The cholesterol level in vehicle, Reelin and DAPT with Reelin treated groups. Each dot represents one individual replicate (n = 3 biological replicates in **C, L, M, O**). Statistical significance was analyzed by One-way ANOVA with Tukey's multiple comparisons test (**C, M, O**). Statistical significance was analyzed by unpaired Student's t test (**L**). For the western blot analysis, similar results were obtained in three independent experiments.

Generation of *Vldlr*-Cre^{ERT2} mice

Vldlr-Cre^{ERT2} mice were generated by homologous recombination at the endogenous *Vldlr* locus using the CRISPR/Cas9 system. Briefly, we inserted *P2A-Cre^{ERT2}* before the stop codon TGA of the *Vldlr* gene. The sgRNA synthesis template was obtained by PCR and purified using the Qiagen MinElute kit with the T7 promoter. The sgRNA sequences were designed as 5'-GACTTGGGAATCCCCTTTTGA-3' and 5'-GGGGCTCAA GGGTTACAGAT-3', and *Cre^{ERT2}* was amplified from addgene13777 by PCR. A mixture of donor DNA plasmid, sgRNA and Cas9 mRNA were microinjected into fertilized zygotes from C57BL/6J females. Injected zygotes were implanted into oviducts of pseudo pregnant ICR female mice. The genotyping primers were 5'-GACTTGGGAATCCCCTTTTGA-3', 5'-GGGGCTCAAAGGGTTACAGAT-3', and 5'-ATCAGCATTCTCCACC ATC-3'. Any potential off-target effects were bred out by backcrossing to C57BL/6 mice for at least five generations before the mice were used for experiments.

Antibodies and reagents

The details for the reagents and antibodies used in this study were listed in Supplementary Table 1 and Table 2.

Plasmid construct and transfection

The pCMV6-NICD-HA plasmid was a gift from Peking Union Medical College, Beijing, China. The pCDN3.1-RELN plasmid was constructed by RuiBiotech (China). The pCMV6-DABI-DDK plasmid and its site-directed mutants were constructed using Gibson assembly technology⁵². Plasmid transfection assay was carried out using the VIGOROUS Transfection System kit (#T001, Vigorous Biotechnology, Beijing, China). For siRNA transfection, cells were transfected with riboFECT CP Transfection Kit (#166 T, RiboBio, China).

Single-cell RNA sequencing

For scRNA-seq sequencing, tendon tissues were harvested from the injury sites of Achilles and Patellar tendons in neonatal (P3) and adult (6-week-old) C57BL/6J mice after 7 days injury. The same age mice were used as control (n = 10 per group, pooled for sequencing). After being washed twice with pre-cooled Phosphate-Buffered Saline (PBS), the collected tissues were cut into 0.5 mm pieces and then digested with 3 mg/mL type I collagenase (Merck, Germany) and 4 mg/mL dispase (Merck, Germany) for 30 min at 37 °C with shaking. After removing erythrocytes with red blood cell (RBC) lysis buffer (Genview, China), the cells were harvested by centrifugation at 450 × g for 15 min at 4 °C, and sequentially filtered through 70 μ m cell strainers. The isolated cells were harvested for library preparation. The library was generated using 10× Genomics Single-Cell V2 Library Construction (Genenergy, Shanghai, China). High-throughput sequencing (Illumina HiSeq PE125/PE150) raw image files were processed by CASAVA base calling to convert into sequenced reads, which were stored in FASTQ format. Mapped RNA-seq reads to the mouse genome (GRCm38) by HISAT2.

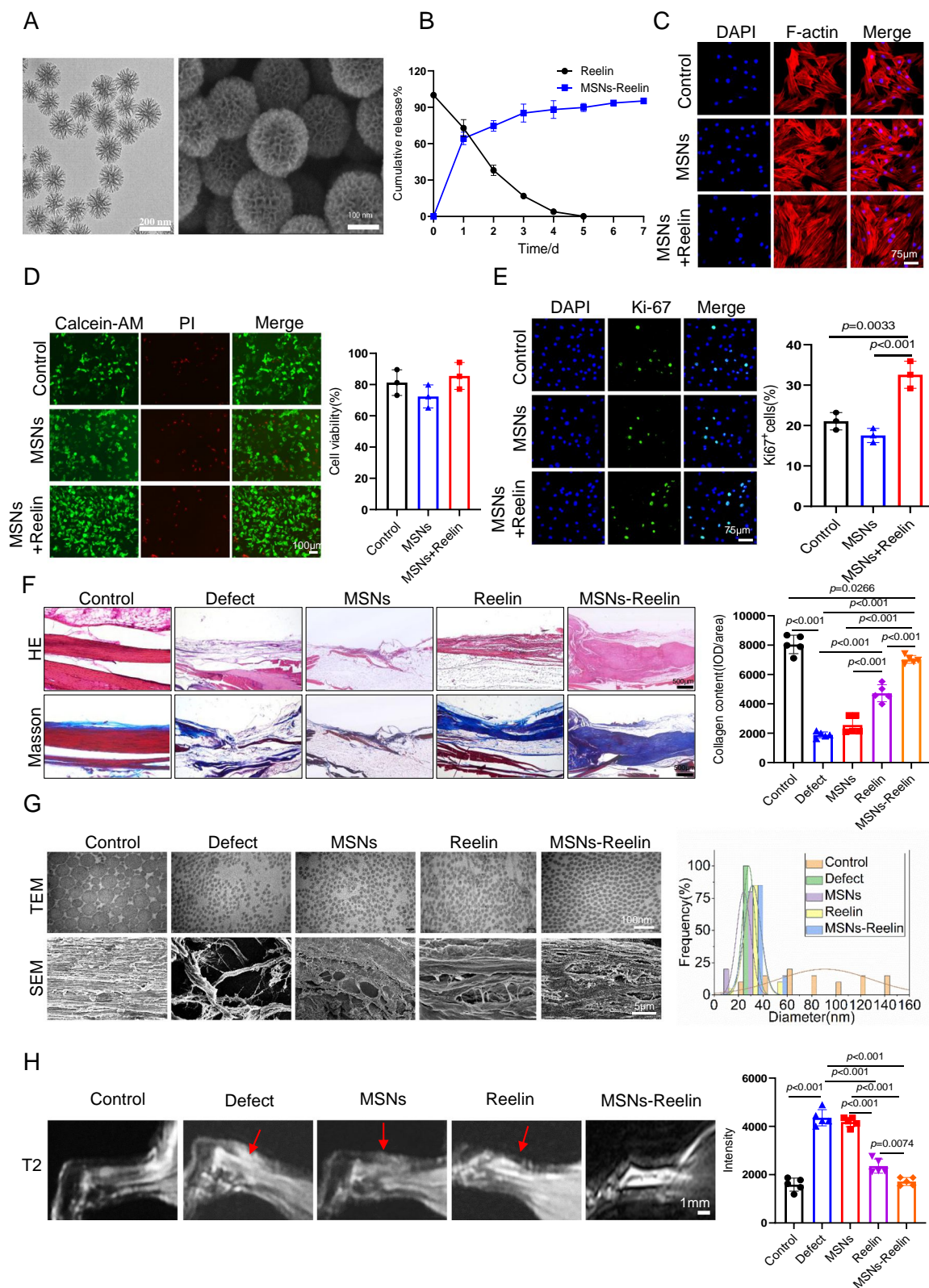
Analysis of scRNA-seq data

For the scRNA-seq data analysis, Seurat (version 3.0.2) was used to normalize the raw counts; Cells with less than 200 genes and mitochondrial gene percentages >15% were removed. After quality control, 25,423 genes from 20,326 neonate cells and 8159 adult cells were selected for further analysis. The filtered batches were integrated using Harmony method. And the scDblFinder function was used to remove doublets. Filtered cells were subjected to dimensionality reduction and clustering by performing RunPCA and RunUMAP functions with dims 1:30. Annotation of cell clusters was based on the most enriched genes and marker genes. For tenogenic subcluster analysis, predefined sets of marker genes identified from published literature were used to identify TSCs, TPCs, and Tenocytes subclusters. Gene sets scores were calculated using the Seurat function AddModuleScore. The gene sets were provided in the source data file. Then CytoTRACE was also used to compare cellular differentiation status of three tenogenic related cell subsets. To quantitatively evaluate the degree of differentiation across cell clusters, a predefined set of stemness-related genes was used to calculate the stemness. The stemness score was calculated by Seurat function AddModuleScore. The stemness-related gene set was provided in the source data file. Next, monocle 3 was used for estimate a pseudotemporal ordering of tendon clusters. And the TSCs subcluster was assigned the root node of the trajectory. The differential genes and enriched clusters among different groups were analyzed by gene ontology (GO) and Kyoto Encyclopedia of Genes and Genomes (KEGG) enrichment analysis. For cell-cell communication analysis, CellChat and CellPhoneDB were employed.

For human tendon samples analysis, one healthy and three pathologic tendon samples at 3 days, 10 days and 12 weeks post-injury were obtained from published datasets (SRA: PRJNA975881, PRJNA976191). The comprehensive donor information was summarized as follows: all samples were obtained from donors aged between 28 and 49 years, with or without tendon injury. Detailed sample informations, including exact age, sex, disease status, and precise time points for sample collection, were presented in Fig. S3C. We performed a re-analysis using the Seurat package. Cells were filtered out with less than 200 expressed genes or mitochondria percentages greater than 20%. The variability across batches were corrected by the Harmony package. PCA was constructed based on the scaled data for the top 2000 high variable genes. And the top 10 principal components were used for UMAP constructions. The cell-cell communication analysis was performed by CellChat and CellPhoneDB.

Bulk RNA-seq analysis

For bulk RNA-seq analysis, *Vldlr*⁺ and *Vldlr*⁻ tendon cells from mice were sorted by flow cytometry and the RNA were extracted using Trizol (#15596026CN, Invitrogen, USA). One microgram of total RNA were used to prepare the sequencing library. Then 2 × 100 paired-end sequencing in fast run mode was performed using the HiSeq 2500 and Illumina TruSeq SBS-Kit v2 (200 cycles). Illumina's bcl2fastq



v1.8.4 software (Illumina, San Diego, CA) was used to convert the resulting base calling (bcl) to FASTQ files. Mapping RNA-seq reads on the mouse genome were performed using DNASTAR Lasergene v15.0 (DNASTAR, Madison, WI) and reported using FPKM (fragments per kilobase of exon per million fragments mapped). Genes with a P -value < 0.05 and fold change > 2 were considered statistically significant. The enrichment of gene clusters and pathways based on

different genes between two groups were performed using Gene Set Enrichment Analysis (GSEA).

Tamoxifen treatment for genetic lineage tracing

Tamoxifen (#10540-29-1, Sigma-Aldrich, USA) was freshly prepared by first dissolving in 100% ethanol and then suspended in corn oil to a final concentration of 20 mg/mL. For tamoxifen induced genetic lineage

Fig. 7 | Slow released Reelin with mesoporous silica nanoparticles promoted tendon regeneration. **A** TEM and SEM images displaying the spherical morphology, highly porous structure, a uniform size of ~190 nm and the cone shaped pores with large opening in MSNs. **B** Reelin release with and without MSNs over the course of 7 days. **C** The cytoskeletons in control, MSNs and MSNs-Reelin groups marked by phalloidin. **D** The live and dead cells in control, MSNs and MSNs-Reelin groups, demonstrated by Calcein-AM and PI staining. **E** The proliferation of TSPCs in control, MSNs and MSNs-Reelin groups, as assessed by Ki67 staining. **F** The HE staining, Masson trichrome staining and collagen content analysis of Achilles tendon in control, defect, MSNs, Reelin and MSNs-Reelin groups 4 weeks postoperatively.

G The collagen fibers arrangement and diameter distribution visualized from cross-sections (upper panel) and longitudinal sections (lower panel) of Achilles tendons in control, defect, MSNs, Reelin and MSNs-Reelin groups, analyzed by TEM and SEM. **H** Sagittal T2-weighted MRI scans of Achilles tendon and the semi-quantitative data in control, defect, MSNs, Reelin and MSNs-Reelin groups. Red arrow: indicate the inflammation signal. Data were presented as Mean \pm SD. $n = 3$ biological replicates per group in (**B**). Each dot represents one individual replicate ($n = 3$ biological replicates per group in (**D**, **E**); $n = 5$ biological replicates in (**F**, **H**)). Statistical significance was analyzed by One-way ANOVA with Tukey's multiple comparisons test (**D**, **E**, **F**, **H**).

tracing, *Prox1-Cre^{ERT2}* mouse lines were used. To induce Cre activity, tamoxifen was intraperitoneal injected at a dose of 7.5 μ l/g body weight for three consecutive days. In all the experiments, tamoxifen injections were performed in both *Cre⁺* and *Cre⁻* mice. At the indicated time, mice were euthanized by CO₂ asphyxiation, and tissues were collected for analysis.

Tendon transection animal model

For mouse tendon transection model, postnatal 3 days (P3) and 6–8 weeks old C57BL/6 mice, P3 old *Reln^{-/-}* mice and *Prox1-Cre^{ERT2}*, *Reln^{fl/fl}* mice were used in this study. Briefly, the Achilles tendon was resected in the middle part. For the regeneration groups, the UV photocuring GelMA with or without TSPCs, Reelin pretreated TSPCs, Reelin, MSNs and Reelin loaded MSNs were grafted into the defect area. Then the incision was suture and bandaged. The mice were provided with unrestricted access to a standard diet and water with free cage activity at constant temperature with a 12 h dark–light cycle. Four weeks postoperatively, the samples were harvested for further investigation ($n = 5$).

To verify the lymphatic vessels expansion after injury, VEGFR3 neutralizing antibodies were used to determine whether this lymphatic vessels expansion was dependent on VEGFR3. Briefly, 100 μ g VEGFR3 neutralizing antibody was injected into the footpads of Achilles tendon resection mouse model every 2 days. The PBS injection ones were used as control. The samples were harvested 7 days postoperatively for further investigation ($n = 5$).

For rabbit tendon regeneration, 4 months old rabbits were used. The Achilles tendon was resected in the middle part. For the regeneration groups, the UV photocuring GelMA combined 4×10^6 TSPCs with or without Reelin loading MSNs was grafted into the defect area. The rabbits were provided with unrestricted access to a standard diet and water with free cage activity at constant temperature with a 12 h dark–light cycle. The samples were harvested after 2 months for further investigation ($n = 5$).

Tendon overuse mouse model

For tendon overuse model establishment, 6–8-week-old *Prox1-Cre^{ERT2}*; *tdTomato* mice were underwent a totally 4-week exercise intervention. Briefly, the intervention start-speed was established at 15 m/min. Exercise intervention consisted of 1 h of running per day, 5 days per week. After 2 weeks exercise, 20 μ l 1% type I collagenase was injected around the Achilles tendon. The Achilles tendons samples were collected two weeks later for the lymphatic distribution analysis.

Indocyanine green (ICG) near-infrared (NIR) lymphatic imaging

Local lymphatic drainage in the Achilles tendon was determined by ICG NIR lymphatic imaging. Briefly, 20 μ l of ICG (#12633, Sigma-Aldrich, USA) at 0.1 mg/ml was injected intradermally into the mouse footpad about 2 mm distal to the calcaneus. ICG imaging of mouse footpads and legs was collected by IVIS Spectrum Small Animal In Vivo Imaging System (PerkinElmer, USA). The signal intensity in the footpad was recorded immediately after ICG injection as the initial signal intensity. ICG imaging was collected again 0.5 h, 1 h, 2 h, 6 h, and 24 h after ICG injection. The images were analyzed using Living Image

software. ICG clearance was quantified as the percentage of reduced ICG signal intensity in the footpad 24 h after injection relative to the initial.

The lymphatic drainage tracer Evans blue injection

To investigate the lymphatic drainage around Achilles tendon, 20 μ l 0.5% Evans blue (G1810, MW 0.96 kDa, Beijing Solarbio Science & Technology Co., Ltd., China) was injected slowly into the mouse footpad about 2 mm distal to the calcaneus of *Prox1-Cre^{ERT2}*; *tdTomato* mice. Then the needle was left in place for approximately 5 min to prevent backflow. The samples were collected for tissue section preparation at 0.5, 1, 2, 6 and 24 h after Evans blue injection.

ELISA assay

The tendon tissues protein was collected by using high-throughput homogenizer. The Reelin ELISA assay kit (#JL33224, Jonlyn, China) was used to detect the reelin concentration according to the manufacturer's instruction. The OD value was measured at a wavelength of 450 nm.

TSPCs subcutaneously transplantation in nude mice

TSPCs (1×10^6 cells) with or without 1 μ g/ml Reelin pretreatment were seeded within GelMA as scaffold, and then implanted subcutaneously into the dorsum of BLAB/c (8-week-old) nude mice. Four weeks later, the implants were harvested for further study.

Achilles functional index analysis

For Achilles functional index (AFI) analysis, a restrictive roadway (59.4 cm long and 42 cm wide) was set using papers as previous report⁵³. Then the mice footprints using red inkpad were recorded and scanned (Epson Scanner, Japan). The following footprints' parameters including print length (PL), toe spreading length (the distance between the first and fifth toes, TS), and intermediary toe spreading length (the distance between the second and fourth toes, IT) were measured. The footprints dimension factors including print length factor (PLF), toe spreading length factor (TSF), and intermediary toe spreading length factor (ITF) were acquired by using the following equations: $PLF = (NPL - EPL)/EPL$, $TSF = (ETS - NTS)/NTS$, $ITF = (EIT - NIT)/NIT$. Finally, AFI was calculated according to the equation: $AFI = 74(PLF) + 161(TSF) + 48(ITF) - 5$.

Histological staining

For H&E staining, the histological sections (5 μ m) were prepared through a microtome and subsequently stained with hematoxylin and eosin following the manufacturer's instruction (G1120, Beijing Solarbio Science & Technology Co., Ltd., China).

For Sirius Red staining, the section was stained with Iron Hematoxylin Staining Solution for 5 min. Then it was stained with Sirius Red Staining Solution for 30 min. Then the images were captured with fluorescence microscope (Olympus VS120, Japan). The collagen content was calculated as follows:

$$\text{Collagen fraction cover area(\%)} = \frac{\text{Cover area of color fraction}}{\text{Total area}} \times 100\%$$

Modified Masson's trichrome staining (G1346, Beijing Solarbio Science & Technology Co., Ltd., China) was performed to examine the maturity of the collagen fibers. Briefly, the section was incubated in Mordant Solution in 57–60 °C incubator for 1 h. Then the section was stained with Celestite Blue Solution, Mayer Hematoxylin Solution, Ponceau-Acid Fuchsin Solution, Phosphomolybic Acid Solution and Aniline Blue Solution for 3–5 min sequentially. The images were acquired by Olympus fluorescence microscope.

Tenogenic differentiation induction

The tenogenic differentiation was induced by a tenogenic differentiation medium, which contained growth medium supplemented with 10 ng/mL TGF- β 1 (Peprotech), 10 ng/mL GDF-5 (R&D System), and 0.05 mM l-ascorbic acid 2-phosphate. After 21-day induction, Sirius Red and Masson's trichrome staining were applied to evaluate tenogenic differentiation capacity, respectively.

Immunofluorescence staining

For immunofluorescence staining, cells were fixed in 4% PFA for 15 min at room temperature. For tendon tissues, frozen histological sections (20 μ m per slice) were prepared. The samples were permeabilized in 0.2% (v/v) TritonX-100 (9002-93-1, BioRuler, USA) for 15 min. Then the samples were incubated with 5% goat serum (ZSGB-BIO) for 1 h. Later the samples were incubated with primary antibody overnight at 4 °C followed by the secondary antibody incubation at room temperature for 1 h. Nuclei were counterstained with DAPI (#C0065, Beijing Solarbio Science & Technology Co., Ltd., China). Confocal microscopic images were acquired with a laser-scanning microscope (Leica TCS SP8, Germany) and then processed with Leica Application Suite X.

The construction of GelMA scaffold

GelMA was purchased from Yongqinuan Intelligent Equipment Co., Ltd. (#EFL-GM-60, Engineering for Life, China). Briefly, GelMA was mixed with 5% photo initiator in a 55 °C water bath. Hydrogel solution was passed through a 0.22 μ m filter, and mixed with cell pellet digested with trypsin-EDTA solution (#25200-072, Gibco, USA) and Reelin (#YBC775Mu01, YBio Biotechnology Co., Ltd, China). After curing under 405 nm light (#EFL-LS-1601-405, Engineering for Life, China) for 15 s. Cells or MSNs were uniformly encapsulated in GelMA. All hydrogels were completely crosslinked.

Scanning electron microscope (SEM)

The tissues were pre-fixed in 2.5% glutaraldehyde in PBS (pH 7.4) at 4 °C for 12 h. Then the samples were dehydrated in a graded series of ethanol (50, 70, 80, 90, 95, and 100%), critical-point dried, and sputter-coated with gold for 2 min at 20 mA. The microstructure of GelMA and regenerated tendon tissues were examined using SEM (Hitachi SU8020, Japan) at 10 kV.

Transmission electron microscopy (TEM)

To detect collagen fibril diameters and alignment, the regenerated tendon samples were prepared following a standard procedure for TEM analysis. Briefly, the samples were fixed with 2.5% glutaraldehyde for 12 h at 4 °C. Then they were fixed with 1% OsO₄ for 1.5 h. Next, the samples were dehydrated by a graded series of acetone (30, 50, 70, 80, and 90%) for about 15 min at each step. Then they were treated with 100% acetone two times, 10 min per times. Then the specimens were placed in order into 1:1 mixture of absolute acetone and resin mixture for 3 h, and into absolute acetone-resin mixture overnight. After that, samples were placed into fresh resin and heated at 70 °C at least for 9 h, and were sliced by LEICA EM UC7 ultratome. Finally, samples were imaged by Hitachi Model H-7650 TEM. Counting and measurement of collagen diameter were processed by marking the fibers individually in Image J 1.52a software.

TESOS clearing, immunolabelling and three-dimensional image acquisition

For tissue clearing, we modified our previous reported protocol to better visualize lymphatic distribution in tendons²⁴. Briefly, the mice were perfused with PBS and 4% PFA. Tendons were fixed in 4% PFA on the shaker overnight. Then they were decalcified in 20% EDTA-Na₂ (pH 7.0) at 37 °C on a shaker for 1 day. Then the samples were decolorized with the Quadrol decolorization solution, gradient tert-butanol (tB) delipidation solutions for 1–2 days, respectively.

For immunolabelling, the pretreated samples were blocked in 5% normal donkey serum (#017-000-121, Jackson ImmunoResearch) for 1 day at 4 °C and incubated with the primary antibody at 4 °C for 4 days. After primary antibody incubation, the samples were washed five times with PBS buffer for 4 h, and then incubated with secondary antibodies at 4 °C for 3 days. Finally, the samples were washed five times over 6 h before clearing. Finally, samples were immersed in the BB-BED medium 47% (v/v) benzyl benzoate (BB), 48% (v/v) bisphenol-A ethoxylate diacrylate Mn 468 (BED) and 5% (v/v) Quadrol and then is supplemented with 2% (w/v) Irgacure 2959 as the UV initiator at room temperature for at least 1 day until transparency was achieved.

For three-dimensional image acquisition, the Leica SP8 confocal microscope equipped with resonant scanner (8000 Hz) and a piezo sample stage (Leica) were used. A magnetic kinematic base (KB25/M or SB1/M, Thorlabs) was used for mounting and transferring samples. Following alignment, embedded samples were mounted on the microtome and sectioned (5 μ m/cut) to expose the sample's top surface. After sectioning, the surface was dropped with a BBPEG immersion medium and imaged. The imaging depth of each imaging z-stack is determined mainly by the objective's working distance.

Magnetic resonance imaging

The regenerated Achilles tendons were measured using an 8-channel surface coil at 3.0T (Philips Ingenia, Philips Healthcare, Netherlands). Acquisition parameters for sagittal T2 were as follows: Turbo spin echo, repetition time = 3104 ms, echo time = 80 ms, field of view = 90 \times 110 mm, matrix size = 384 \times 384, slice thickness = 1 mm.

Mechanical property analysis

Mechanical property was conducted using an Instron tension/compression system with Fast-Track software (Model 5969, Instron, Canton, MA). The Achilles complexes harvested at 4 weeks postoperatively were wrapped in gauze soaked in saline. Before testing, the Achilles complexes were gradually thawed at room temperature, and all surrounding soft tissues were rigorously removed. Measurements of the tendon cross-sectional area were performed using aqueous rapid curing alginate dental impression paste. The complex was then fixed to custom-made clamps using high strength thread. After applying a preload of 0.1 N, each complex was cyclically elongated between 0 and 0.5 mm for 20 cycles at 5 mm/min in advance. The load-elongation behavior of the complex and failure modes was recorded. The structural properties of the complex were calculated by modulus (MPa) and stress at failure (MPa).

Stem cell isolation and culture

Primary TSPCs were isolated from P3, 6–8-week-old mice and 2–4 month-old rabbits according to previously established procedure. Briefly, the harvested Achilles tendon was cut into small pieces and digested in 3 mg/mL Type I collagenase (Merck) and 4 mg/mL dispase (Merck) at 37 °C for 30 min to get the single cell suspension. After centrifugation at 400 \times g for 5 min, cells were resuspended and cultured in low-glucose Dulbecco's modified Eagle's medium (DMEM, Gibco) supplemented with 20% fetal bovine serum (FBS, Gibco) and 100 U/mL penicillin/streptomycin (Hyclone). After growing to 80–90% confluence, cells were passaged with fresh medium. The passage 2–4 TSPCs were used for further experiments.

For *Vldlr*⁺ and *Vldlr*⁻ TSPCs isolation, tendon cells were firstly isolated from *Vldlr*-Cre^{ERT2}; tdTomato mice after 7 days of tamoxifen induction at P3–P5. Then the cells were stained with COL1 α 1 antibody, followed by the FITC-conjugated secondary antibody staining. Then the *Vldlr*⁺ and *Vldlr*⁻ TSPCs among COL1 α 1 positive cells were sorted by BD Aria SORP (BD Biosciences, USA).

Cell viability staining

For cell viability analysis, the live/dead cells were stained according to the manufacturer's protocol (Beijing Solarbio Science & Technology Co., Ltd., China). Briefly, cells were incubated 30 min with 2 μ M calcein-AM and 4.5 μ M Propidium iodide dissolved in PBS. Then the images were acquired with Olympus fluorescence microscope.

Western blotting

Total proteins from cell lysates were harvested by RIPA Buffer with Protease/Phosphatase Inhibitor Phenylmethylsulfonyl fluoride (PMSF) (#P0100, Beijing Solarbio Science & Technology Co., Ltd., China). Nuclear and cytoplasmic proteins were extracted with Nuclear Protein Extraction Kit (#P0027, Beyotime, China). Proteins were separated by 4–15% SDS-polyacrylamide gel electrophoresis (SDS-PAGE), and then transferred to polyvinylidene difluoride membranes (PVDF) and blocked in 5% nonfat milk. The membranes were probed with corresponding primary antibodies overnight at 4 °C. Then the secondary antibodies were incubated for 1 h at room temperature. After the membranes were enhanced with SuperSignal West Pico Chemiluminescent Substrate (#34077, Invitrogen, USA), The bands were detected by Imaging System (Bio-Rad, USA). GAPDH antibody was used to quantify the amount of loaded protein. The uncropped and unprocessed blots are provided in Source Data file.

Co-immunoprecipitation (Co-IP) analysis

For co-immunoprecipitation assay, cells were lysed with lysis buffer (#9803, Cell Signaling Technology, USA) for 30 min on ice. Then the cell lysate was centrifuged with 12,000 \times g for 10 min and supernatant was incubated with antibodies overnight at 4 °C, followed by Protein A/G agarose (#sc-2003, Santa Cruz Biotechnology, USA) incubation for 2 h at 4 °C. The Anti-HA Rabbit mAb was used for NICD-HA protein immunoprecipitation. The Anti-SREBP2 Rabbit mAb, Anti-DAB1 Rabbit mAb, and Anti-VLDLR Rabbit mAb were used for SREBP2, DAB1 and VLDLR protein immunoprecipitation, respectively. The precipitated protein was collected by centrifugation (4000 \times g for 5 min at 4 °C). After washing, precipitated proteins were denatured (100 °C for 5 min) and separated by SDS-PAGE, then detected by immunoblotting following the western blotting protocol.

RT-qPCR

For RT-qPCR analysis, tendon tissues or cultured cells were harvested using Trizol to obtain RNA. Then the 1 μ g RNA was reverse-transcribed into cDNA with the ReverTra Ace[®] qPCR RT Master Mix Kit (#420600, Toyobo, Japan). Then 0.5 μ g cDNA per sample were used to perform qPCR using gene-specific primers and SYBR Green Premix PRO Taq HS Quantitative PCR Kit II (AG11719, Accurate Biology, China) on 7900HT Fast Time PCR. The primers were listed in Supplementary Table 3.

SiRNA knockdown

To knock down *Dab1* or *Srebp2* in TSPCs, siRNA transfection was performed according to the manufacturer's instructions (C10511-05, RiboBio, China). Briefly, the riboFECT[™] CP was added into the low-glucose Dulbecco's modified eagle medium (L-DMEM) without penicillin-streptomycin solution. The siRNA oligonucleotide sequences used were listed in Supplementary Table 4. In 21-day tenogenic differentiation induction assay, the transfection complex was added every 3 days with the induction medium change. On day 2 and 21 post-

transfection, *Srebp2* and *Dab1* mRNA levels were quantified by RT-qPCR to assess knockout efficiency.

Synthesis of surface modified mesoporous silica nanoparticles

Mesoporous silica nanoparticles (MSNs) were synthesized via the sol-gel method within an oil-water system^{36,37}. In a typical synthesis, a water phase comprising 60 mL was prepared by blending 24 mL of cetyltrimethylammonium chloride (CTAC) (25% aqueous solution), 0.20 g of triethylamine (TEA), and 736 mL of MilliQ ultra-pure water at 60 °C for 1 h. Subsequently, 40 mL of the oil phase, consisting of 37.5 mL of chlorobenzene and 2.5 mL of tetraethyl orthosilicate (TEOS), was gently introduced into the bottom of the water phase. The resulting mixture was stirred at 60 °C with a stirring speed of 500 g for 12 h. The solid samples were then subjected to centrifugation at 18,522 \times g for 15 min and washed thrice with ethanol. Finally, the MSNs products underwent calcination at 550 °C for 5 h to eliminate the organic surfactant.

In the subsequent step, MSNs was functionalized with polyethyleneimine (PEI). Initially, 60 mg of MSNs was dispersed in 15 mL of MilliQ water, and the pH was adjusted to 10. Following this, 15 mL of N-(3-(trimethoxysilyl) propyl) ethylenediamine (THPMP) solution (56 mM) was added, and the mixture was stirred at 40 °C for 2 h. The particles were then collected via centrifugation at 18,522 g for 15 min and washed thrice with water. Subsequently, the product was suspended in a PEI solution (10 mg/mL in 100 mM carbonate buffer, pH = 9.6) and stirred for 4 h at room temperature. The final product underwent thorough washing with water and was air-dried at room temperature.

For the preparation of MSNs solution, nanoparticles were dispersed in PBS with a final concentration of 1 mg/mL with ultrasonic treatment. For Reelin protein loading in MSNs, 10 μ L protein solution (200 μ g/mL) was mixed with 10 μ L silica nanoparticles (200 μ g/mL) with gentle shaking for 24 h at 4 °C.

Characterization of surface modified mesoporous silica nanoparticles

For MSNs characterization, the powder samples were dispersed in ethanol, dropped onto an aluminum foil piece, and affixed to a conductive carbon film. Following this, the samples were subjected to drying in a vacuum oven at 60 °C for 12 h and subsequently cleaned with an Evactron 25/45 De-contaminator RF plasma cleaning system. Then the morphology and pores of MSNs were analyzed by SEM and TEM.

Nitrogen adsorption-desorption measurements were conducted at -196 °C with a Micromeritics Tristar II system, before testing the samples were degassed at 100 °C overnight on a vacuum line. The total pore volume was calculated from the amount adsorbed at a maximum relative pressure (P/P₀) of 0.99. The Barrett-Joyner-Halenda (BJH) method was used to calculate the pore size of samples from the adsorption branches of the isotherms. The Brunauer-Emmett-Teller (BET) method was utilized to calculate the specific surface areas. Dynamic light scattering (DLS) was carried out at 25 °C using a Zetasizer Advance Series- Pro from Malvern Panalytical Ltd.

Measurement of cholesterol

The cholesterol level was detected by Amplex Red Cholesterol and Cholesteryl Ester Assay Kit according to the manufacture's instruction (#S0211M, Beyotime, China). Briefly, the cells were collected by centrifuged (500 \times g for 5 min) and the supernatant was discarded. Then the buffer A was added to the sample and mixed well. The supernatants were collected by centrifugation (12,000 \times g for 5 min at 4 °C) for absorbance detection at 570 nm using multifunctional microplate reader (BioTek Synergy H1 Multimode Reader, Agilent, USA). The cholesterol level was quantified relative to the standard.

Cleavage under targets and tagmentation (CUT&Tag)

We performed chromatin immunoprecipitation with a NovoNGS CUT&Tag High-Sensitivity kit (N259-YH01, Novoprotein, China) following the manufacturer's protocol. In brief, 100,000 cells were harvested, crosslinked with 1% formaldehyde, and permeabilized. The proteins DNA complex were then bound to ConA magnetic beads and incubated overnight at 4 °C with anti-Notch1 antibody or IgG isotype control for immunoprecipitation. After subsequent incubation with secondary antibodies, the immunoprecipitated DNA was purified from beads and analyzed by qPCR. Primer sequences used can be found in Supplementary Table 5.

Statistical analysis

The quantitative data were presented using the mean ± standard deviation (SD). Statistical analysis was performed with GraphPad Prism10. The comparison between two groups was analyzed by independent unpaired two tailed Student's *t* tests, and comparisons among more than two groups were conducted using one-way analysis of variance (ANOVA) with Tukey's multiple comparisons test. *P* < 0.05 were statistically significant.

Reporting summary

Further information on research design is available in the Nature Portfolio Reporting Summary linked to this article.

Data availability

The bulk RNA seq data is deposited in the GEO under the accession code [GSE282034](https://www.ncbi.nlm.nih.gov/bioproject/PRJNA975881). The scRNA-seq data are deposited in GEO repository under the accession code [GSE286346](https://www.ncbi.nlm.nih.gov/bioproject/PRJNA976191). The referenced human tendon sample datasets were obtained from published datasets (SRA: PRJNA975881, PRJNA976191) [<https://www.ncbi.nlm.nih.gov/bioproject/?term=PRJNA975881>] [<https://www.ncbi.nlm.nih.gov/bioproject/PRJNA976191>]²⁹. Source data are provided with this paper.

References

- Peserico, A. et al. Mammal comparative tendon biology: advances in regulatory mechanisms through a computational modeling. *Front. Vet. Sci.* **10**, 1175346 (2023).
- Tang, C. et al. Classification of distinct tendinopathy subtypes for precision therapeutics. *Nat. Commun.* **15**, 9460 (2024).
- Grinstein, M. et al. A latent axin2(+)/Scx(+) progenitor pool is the central organizer of tendon healing. *NPJ Regen. Med.* **9**, 30 (2024).
- Bi, Y. et al. Identification of tendon stem/progenitor cells and the role of the extracellular matrix in their niche. *Nat. Med.* **13**, 1219–1227 (2007).
- Sripathi, P. & Agrawal, D. K. Rotator cuff injury: pathogenesis, biomechanics, and repair. *J. Orthop. Sports Med.* **6**, 231–248 (2024).
- Sankova, M. V. et al. Recent developments in Achilles tendon risk-analyzing rupture factors for enhanced injury prevention and clinical guidance: current implications of regenerative medicine. *J. Orthop. Transl.* **49**, 289–307 (2024).
- Ackerman, J. E. et al. Defining the spatial-molecular map of fibrotic tendon healing and the drivers of Scleraxis-lineage cell fate and function. *Cell Rep.* **41**, 111706 (2022).
- Huang, A. H. et al. Requirement for scleraxis in the recruitment of mesenchymal progenitors during embryonic tendon elongation. *Development* **146**, dev182782 (2019).
- Lee, C. H. et al. Harnessing endogenous stem/progenitor cells for tendon regeneration. *J. Clin. Investig.* **125**, 2690–2701 (2015).
- Fan, C. et al. A Cd9(+)/Cd271(+) stem/progenitor population and the SHP2 pathway contribute to neonatal-to-adult switching that regulates tendon maturation. *Cell Rep.* **39**, 110762 (2022).
- Harvey, T., Flamenco, S. & Fan, C. M. A Tppp3(+)/Pdgfra(+) tendon stem cell population contributes to regeneration and reveals a shared role for PDGF signalling in regeneration and fibrosis. *Nat. Cell Biol.* **21**, 1490–1503 (2019).
- Tempfer, H. et al. Presence of lymphatics in a rat tendon lesion model. *Histochem. Cell Biol.* **143**, 411–419 (2015).
- Tong, X. et al. Rotator cuff healing is regulated by the lymphatic vasculature. *J. Orthop. Transl.* **38**, 65–75 (2023).
- Niec, R. E. et al. Lymphatics act as a signaling hub to regulate intestinal stem cell activity. *Cell Stem Cell* **29**, 1067–1082.e18 (2022).
- Bernier-Latmani, J. & Petrova, T. V. Intestinal lymphatic vasculature: structure, mechanisms and functions. *Nat. Rev. Gastroenterol. Hepatol.* **14**, 510–526 (2017).
- D'Arcangelo, G. & Curran, T. Reeler: new tales on an old mutant mouse. *Bioessays* **20**, 235–244 (2015).
- Santana, J. & Marzolo, M.-P. The functions of Reelin in membrane trafficking and cytoskeletal dynamics: implications for neuronal migration, polarization and differentiation. *Biochem. J.* **474**, 3137–3165 (2017).
- Liu, X. et al. Lymphoangiocrine signals promote cardiac growth and repair. *Nature* **588**, 705–711 (2020).
- Jausoro, I. & Marzolo, M. P. Reelin activates the small GTPase TC10 and VAMP7 to promote neurite outgrowth and regeneration of dorsal root ganglia (DRG) neurons. *J. Neurosci. Res.* **99**, 392–406 (2021).
- Dou, A., Zhang, Y., Wang, Y., Liu, X. & Guo, Y. Reelin depletion alleviates multiple myeloma bone disease by promoting osteogenesis and inhibiting osteolysis. *Cell Death Discov.* **7**, 219 (2021).
- Howell, K. et al. Novel model of tendon regeneration reveals distinct cell mechanisms underlying regenerative and fibrotic tendon healing. *Sci. Rep.* **7**, 45238 (2017).
- Rao, Y. et al. Tenogenic induction of human adipose-derived stem cells by soluble tendon extracellular matrix: composition and transcriptomic analyses. *Stem Cell Res. Ther.* **13**, 380 (2022).
- Huang, S. et al. Non-collagenous proteins, rather than the collagens, are key biochemical factors that mediate tenogenic bioactivity of tendon extracellular matrix. *Acta Biomater.* **176**, 99–115 (2024).
- Yi, Y. et al. Mapping of individual sensory nerve axons from digits to spinal cord with the transparent embedding solvent system. *Cell Res.* **34**, 124–139 (2024).
- Antila, S. et al. Development and plasticity of meningeal lymphatic vessels. *J. Exp. Med.* **214**, 3645–3667 (2017).
- Li, Z. et al. Blockade of VEGFR3 signaling leads to functional impairment of dural lymphatic vessels without affecting auto-immune neuroinflammation. *Sci. Immunol.* **8**, eabq0375 (2023).
- Zhang, D. et al. Targeting local lymphatics to ameliorate heterotopic ossification via FGFR3-BMP1a pathway. *Nat. Commun.* **12**, 4391 (2021).
- Yoon, J. H. et al. Nasopharyngeal lymphatic plexus is a hub for cerebrospinal fluid drainage. *Nature* **625**, 768–777 (2024).
- Zhang, X. et al. Multi-omics analysis of human tendon adhesion reveals that ACKR1-regulated macrophage migration is involved in regeneration. *Bone Res.* **12**, 27 (2024).
- Marshall, B. P. et al. The subacromial bursa modulates tendon healing after rotator cuff injury in rats. *Sci. Transl. Med.* **16**, eadd8273 (2024).
- Lopera, F. et al. Resilience to autosomal dominant Alzheimer's disease in a Reelin-COLBOS heterozygous man. *Nat. Med.* **29**, 1243–1252 (2023).
- Gao, Z. & Godbout, R. Reelin-Disabled-1 signaling in neuronal migration: splicing takes the stage. *Cell. Mol. Life Sci.* **70**, 2319–2329 (2013).
- Hashimoto-Torii, K. et al. Interaction between reelin and notch signaling regulates neuronal migration in the cerebral cortex. *Neuron* **60**, 273–284 (2008).

34. Yagyu, H. et al. Very low density lipoprotein (VLDL) receptor-deficient mice have reduced lipoprotein lipase activity. Possible causes of hypertriglyceridemia and reduced body mass with VLDL receptor deficiency. *J. Biol. Chem.* **277**, 10037–10043 (2002).
35. Gu, Q. et al. AIBP-mediated cholesterol efflux instructs hematopoietic stem and progenitor cell fate. *Science* **363**, 1085–1088 (2019).
36. Li, H. et al. Nanotherapy in joints: increasing endogenous hyaluronan production by delivering hyaluronan synthase 2. *Adv. Mater.* **31**, e1904535 (2019).
37. Xu, C. et al. Core-cone structured monodispersed mesoporous silica nanoparticles with ultra-large cavity for protein delivery. *Small* **11**, 5949–5955 (2015).
38. Vinestock, R. C. et al. Neonatal entheses healing involves noninflammatory acellular scar formation through extracellular matrix secretion by resident cells. *Am. J. Pathol.* **192**, 1122–1135 (2022).
39. Gur-Cohen, S. et al. Stem cell-driven lymphatic remodeling coordinates tissue regeneration. *Science* **366**, 1218–1225 (2019).
40. Harvey, N. L. Lymphatic vessels as a stem cell niche. *Science* **366**, 1193–1194 (2019).
41. Sawahata, M. et al. Generation and analysis of novel Reelin-deleted mouse model corresponding to exonic Reelin deletion in schizophrenia. *Psychiatry Clin. Neurosci.* **74**, 318–327 (2020).
42. Lutter, S., Xie, S., Tatin, F. & Makinen, T. Smooth muscle-endothelial cell communication activates Reelin signaling and regulates lymphatic vessel formation. *J. Cell Biol.* **197**, 837–849 (2012).
43. Ma, L. et al. Skull progenitor cell-driven meningeal lymphatic restoration improves neurocognitive functions in craniostosis. *Cell Stem Cell* **30**, 1472–1485.e7 (2023).
44. Khialeeva, E. et al. Reelin deficiency delays mammary tumor growth and metastatic progression. *J. Mammary Gland Biol. Neoplasia* **22**, 59–69 (2017).
45. Cho, D. I. et al. Mesenchymal stem cells reciprocally regulate the M1/M2 balance in mouse bone marrow-derived macrophages. *Exp. Mol. Med.* **46**, e70 (2014).
46. Alitalo, K. The lymphatic vasculature in disease. *Nat. Med.* **17**, 1371–1380 (2011).
47. Steffen, D., Mienaltowski, M. & Baar, K. Spatial gene expression in the adult rat patellar tendon. *Matrix Biol. Plus* **19–20**, 100138 (2023).
48. Still, C. et al. Single-cell transcriptomic profiling reveals distinct mechanical responses between normal and diseased tendon progenitor cells. *Cell Rep. Med.* **2**, 100343 (2021).
49. Yin, Z. et al. Single-cell analysis reveals a nestin(+) tendon stem/progenitor cell population with strong tenogenic potentiality. *Sci. Adv.* **2**, e1600874 (2016).
50. Luo, Z. et al. NUMB enhances Notch signaling by repressing ubiquitination of NOTCH1 intracellular domain. *J. Mol. Cell Biol.* **12**, 345–358 (2020).
51. Wu, Q. et al. Methotrexate and Triptolide regulate Notch signaling pathway by targeting the Nedd4-Numb axis. *Int. Immunopharmacol.* **114**, 109595 (2023).
52. Gibson, D. G. et al. Enzymatic assembly of DNA molecules up to several hundred kilobases. *Nat. Methods* **6**, 343–345 (2009).
53. Yang, S. et al. Oriented collagen fiber membranes formed through counter-rotating extrusion and their application in tendon regeneration. *Biomaterials* **207**, 61–75 (2019).

Acknowledgements

This work was supported by the National Key Research and Development Program of China No. 2022YFA1105800 (R.Y.), Joint Program on

Health Science&Technology Innovation of Hainan Province No.193 (R.Y.), the Fundamental Research Funds for the Central Universities—Peking University Clinical Scientist Training Program No. PKU2024LCXQ016 (R.Y), and Clinical Medicine Plus X-Young Scholars Project of Peking University. No. 2024 (R.Y.).

Author contributions

R.L. Yang contributed to conception and design, data acquisition, analysis, and interpretation, and critically revised the manuscript; L.C. and M.C. contributed to design, data analysis and interpretation, critically revised the manuscript; S.L., M.L., Z.Z., and H.Z. contributed to data analysis, critically revised the manuscript; H.Z. contributed to tissue clearing technology instruction and critically revised the manuscript. C.X. contributed to nano particles synthesis and critically revised the manuscript. All authors gave final approval and agree to be accountable for the work.

Competing interests

The authors declare no competing interests.

Additional information

Supplementary information The online version contains supplementary material available at <https://doi.org/10.1038/s41467-025-67898-9>.

Correspondence and requests for materials should be addressed to Ruili Yang.

Peer review information *Nature Communications* thanks Ruijian Yan and the other anonymous reviewer(s) for their contribution to the peer review of this work. A peer review file is available.

Reprints and permissions information is available at <http://www.nature.com/reprints>

Publisher's note Springer Nature remains neutral with regard to jurisdictional claims in published maps and institutional affiliations.

Open Access This article is licensed under a Creative Commons Attribution-NonCommercial-NoDerivatives 4.0 International License, which permits any non-commercial use, sharing, distribution and reproduction in any medium or format, as long as you give appropriate credit to the original author(s) and the source, provide a link to the Creative Commons licence, and indicate if you modified the licensed material. You do not have permission under this licence to share adapted material derived from this article or parts of it. The images or other third party material in this article are included in the article's Creative Commons licence, unless indicated otherwise in a credit line to the material. If material is not included in the article's Creative Commons licence and your intended use is not permitted by statutory regulation or exceeds the permitted use, you will need to obtain permission directly from the copyright holder. To view a copy of this licence, visit <http://creativecommons.org/licenses/by-nc-nd/4.0/>.

© The Author(s) 2025